NEOPLASMA accepted, ahead of print manuscript
Cite article as https://doi.org/10.4149/neo_2026_260518N157

Running title: Three-gene prognostic signature in follicular lymphoma

Prognostic value of cell differentiation-related genes in follicular lymphoma based on integrated single-cell and bulk RNA sequencing

Xiaoyu Xiang[1,*], Wu Deng[2,3,*]

[1]Department of Critical Care Medicine, West China Hospital of Sichuan University, Chengdu, Sichuan, China; [2]Department of Pediatrics, Key Laboratory of Birth Defects and Related Diseases of Women and Children Sichuan University, Chengdu, Sichuan, China; [3]Ministry of Education, West China Second University Hospital, Sichuan University, Chengdu, Sichuan, China

*Correspondence: xxy071796@163.com; 18200239065@163.com

Received May 18, 2026 / Accepted October 12, 2026

Follicular lymphoma (FL) is the most common indolent B-cell lymphoma and follows a heterogeneous clinical course; however, reliable molecular markers for risk stratification are still lacking. We integrated single-cell RNA sequencing data (GSE182434) with bulk transcriptomic data from three GEO cohorts (GSE66166, GSE119214, GSE16131) and applied pseudotime trajectory analysis, consensus clustering, weighted gene co-expression network analysis, and LASSO Cox regression to derive a cell differentiation-related gene signature (CDRGS) and a prognostic risk model. Model performance was evaluated by time-dependent ROC analysis, the concordance index, calibration curves, decision-curve analysis, and multivariable Cox regression, and the expression of the signature genes was examined by RT-qPCR, western blot, and immunohistochemistry in lymphoma cell lines, in a SU-DHL-4 xenograft model, and in an independent cohort of patients with FL. Pseudotime analysis resolved three differentiation states, and consensus clustering based on the CDRGS stratified patients into three molecular subtypes with different overall survival. A three-gene model comprising SIRPG, FLT3LG, and LAG3 separated high- and low-risk patients in the training cohort and in the GSE119214 validation cohort, with separation in the same direction but not reaching significance in GSE16131, and remained associated with overall survival after adjustment for M7-FLIPI in the two cohorts in which that index was available. All three genes were expressed at higher mRNA and protein levels in lymphoma cell lines than in a non-malignant B lymphoblastoid line, indicating that the malignant cells themselves express them. In an independent patient cohort, the expression of the three-gene panel varied with risk score and with established clinical indices in the directions predicted by the model coefficients. We constructed a cell differentiation-related prognostic model for FL and found that SIRPG, FLT3LG, and LAG3 provide candidate biomarkers of the immune microenvironment that carry prognostic information beyond M7-FLIPI and merit prospective validation.

Key words: prognostic model; follicular lymphoma; single-cell sequencing; SIRPG/FLT3LG/LAG3; biomarker

Follicular lymphoma (FL) is the most common indolent B-cell lymphoma in Western countries and originates from germinal center B cells. A substantial proportion of FL patients undergo histological

transformation to the more aggressive diffuse large B-cell lymphoma (DLBCL) during the course of disease, which is often accompanied by rapid progression, treatment resistance, and poor survival [1-3]. Although recent studies have linked FL transformation to specific gene mutations and changes in the tumor microenvironment (TME), no reliable biomarker for predicting the risk of transformation has been established [4, 5]. Mounting evidence indicates that small but biologically distinct cell subsets within FL contribute disproportionately to disease aggressiveness [6, 7]. Gene expression signatures enriched in macrophages and follicular dendritic cells have been associated with poor prognosis, whereas T cell-enriched signatures correlate with favorable outcomes [8-11], suggesting that crosstalk between lymphoma cells and the surrounding stromal and immune compartments is a key driver of disease progression [12, 13]. The dynamic interplay between immune surveillance and the TME further shapes the clinical course of FL [14, 15]. A more comprehensive characterization of tumor cell diversity and immune microenvironment composition is therefore needed to identify reliable prognostic markers and potential therapeutic targets for FL.

Single-cell RNA sequencing (scRNA-seq) has emerged as a powerful tool for dissecting tumor heterogeneity and evolutionary dynamics by profiling whole-transcriptome expression at single-cell resolution. This technology enables the identification of hidden cellular subpopulations, the characterization of immune microenvironment composition, and the elucidation of biological features that distinguish different cell populations within a tumor. Previous scRNA-seq studies have characterized intratumoral heterogeneity in FL and the crosstalk between malignant B cells and surrounding infiltrating lymphocytes. Andor et al. applied scRNA-seq to distinguish tumor-infiltrating normal B cells from malignant B cells and demonstrated that infiltrating T cells express high levels of immune checkpoint genes [16]. Roider et al. used scRNA-seq to reveal intratumoral heterogeneity in FL at the transcriptional, genetic, and drug response levels [17]. Despite these advances, prognostic gene signatures derived from the integration of scRNA-seq and bulk transcriptomic data remain scarce in FL.

Given the need for robust prognostic biomarkers in FL, this study aimed to identify a cell differentiation-related gene signature (CDRGS) and to construct a multi-cohort prognostic risk model by integrating single-cell and bulk transcriptomic data. scRNA-seq analysis, pseudotime trajectory analysis, and single-sample gene set enrichment analysis (ssGSEA) were applied to dissect cellular heterogeneity and to derive the CDRGS. Consensus clustering of the CDRGS defined three molecular subtypes, and comparison of the ESTIMATE and CIBERSORT immune infiltration profiles between these subtypes identified the immune populations that were used as traits in weighted gene co-expression network analysis (WGCNA), from which a co-expression module and its hub genes were

extracted. These hub genes were refined by least absolute shrinkage and selection operator (LASSO) Cox regression to derive a three-gene risk score, which was then evaluated in two external cohorts. Expression of the three risk genes was further examined by quantitative real-time PCR (RT-qPCR), Western blot, and immunohistochemistry in lymphoma cell lines, in SU-DHL-4 xenograft tumors, and in diagnostic lymph node specimens from an independent cohort of patients with FL. This study provides a candidate prognostic tool for FL and offers biomarkers for further mechanistic and translational investigation.

Patients and methods

Data acquisition. Public transcriptomic and clinical data for follicular lymphoma (FL) were retrieved from the Gene Expression Omnibus (GEO; https://www.ncbi.nlm.nih.gov/geo/) database (Table 1), following an integrative strategy comparable to that reported previously [18]. The scRNA-seq dataset GSE182434 was used to characterize the FL tumor microenvironment, and 18,570 genes from 3,831 cells were retained after excluding DLBCL and normal tonsil samples; these cells then entered the quality-control step described below. GSE66166 (GPL13938, Illumina HumanHT-12 WG-DASL V4.0 expression beadchip), containing mRNA expression profiles and clinical information from 138 FL patients, was used as the training cohort for prognostic model construction; 106 of these samples had complete overall survival and clinical annotation, and all survival analyses, model derivation and model evaluation in this cohort were therefore performed in these 106 patients. GSE119214 (GPL13938, Illumina HumanHT-12 WG-DASL V4.0 expression beadchip, n=137) and GSE16131 (GPL96/ GPL97, [HG-U133A] Affymetrix Human Genome U133A Array/[HG-U133B] Affymetrix Human Genome U133B Array, n=180) served as external validation cohorts. The clinical variables available in each cohort and the proportion of non-missing values for each variable are summarized in Supplementary Table S1. Complete-case analysis was used for all models involving clinical covariates, and no imputation was performed.

Patient specimens and independent clinical cohort. Diagnostic lymph node specimens from patients with newly diagnosed follicular lymphoma were collected at West China Second University Hospital, Sichuan University, between January 2022 and December 2025. The Institutional Ethics Committee approved the study and waived informed consent because it was retrospective and used archived paraffin-embedded tissue (Approval 2021-190). Diagnoses followed the fifth edition of the World Health Organization classification of hematolymphoid tumors and were reviewed by two hematopathologists. Histological grade (1-2 as low grade, 3A as high grade), Ann Arbor stage, FL-IPI, end-of-treatment Deauville score and BCL2/BCL6 status by fluorescence in situ hybridization were

retrieved from the clinical records; cases were classified as altered if a BCL2 or BCL6 rearrangement, including BCL2/IGH fusion, was detected. The endpoint was event-free survival, from the start of first-line treatment to refractory disease, relapse, or histological transformation, with responding patients censored at last follow-up (median follow-up 14 months). RNA of adequate quality was not available for every specimen, so the number of evaluable cases differs between analyses and is reported for each comparison in the Results. Patients were dichotomized at the cohort median expression of the gene concerned; the risk score was calculated for the 24 patients with complete expression data for all three genes using the GSE66166 coefficients applied to expression values z-scored within this cohort, and dichotomized at the cohort median (0.0524). This cohort was not used in model derivation.

scRNA-seq data preprocessing and quality control. Raw single-cell count matrices for FL were downloaded from GSE182434, and Seurat objects were created in R using the Seurat package. Standard quality filters were applied to remove low-quality cells and potential doublets: cells with fewer than 200 or more than 6,000 detected genes, or with mitochondrial gene content exceeding 5%, were excluded (Supplementary Figure S1A). This step retained 3,793 cells, and gene expression was subsequently normalized using the NormalizeData() function.

Dimensionality reduction, clustering, and cell type annotation. The top 2,000 highly variable genes were identified using FindVariableFeatures() (Supplementary Figure S1B), centered and scaled with ScaleData(), and used as input for principal component analysis (PCA) via RunPCA(). The optimal number of principal components was determined by inspecting JackStrawPlot() and ElbowPlot() outputs **(**Supplementary Figures S1C, S1D), and the top 20 PCs were retained for downstream analysis. Graph-based clustering was performed using FindClusters() at a resolution of 0.9, and t-distributed stochastic neighbor embedding (t-SNE) was applied for two-dimensional visualization. Cluster-specific marker genes were identified using FindAllMarkers() with the following parameters: only.pos=FALSE, min.pct=0.25, $|\log FC| > 1$, and adjusted $p < 0.05$ [19]. Cell type annotation was performed by mapping the clusters against the "ref_Monaco_114s.RData" reference dataset, with both assay.type.test and assay.type.ref set to "logcounts" (Supplementary Figure S2).

Pseudotime trajectory analysis. Single-cell trajectory analysis was performed to delineate developmental dynamics among the tumor cell populations using the Monocle2 R package [20] with default settings. Differential expression testing for state-associated genes was conducted using the FindMarkers() function in Seurat, and significant genes were retained based on $|\log FC| > 1$ and adjusted $p < 0.05$. To characterize how the expression of the CDRGS genes changed along the branched trajectory, branched expression analysis modeling (BEAM) was performed on the CDRGS genes using the BEAM() function in Monocle 2 at branch point 1, which resolves States 2 and 3;

BEAM fits a negative binomial generalized additive model allowing gene expression to vary as a smooth function of pseudotime independently in each branch and compares it by likelihood ratio test to a null model in which expression varies with pseudotime but not with branch identity. Genes with a BEAM adjusted p-value (qval) below 0.05 were considered branch-dependent, and genes were ranked by adjusted P-value and visualized using plot_genes_branched_heatmap() (Supplementary Figure S3).

Derivation of the cell differentiation-related gene signature (CDRGS). The CDRGS was derived from the pseudotime analysis through the following sequential filtering steps, with the number of genes retained at each stage shown in Supplementary Figure S4. Differential expression testing between clusters identified 1,604 genes ($|\log FC| > 1$, adjusted $p < 0.05$; Supplementary Table S2), which were used as the ordering feature set for Monocle 2 and resolved three pseudotime states. Differential expression testing across these three states, applying the same thresholds, yielded 394 genes, which constitute the CDRGS (Supplementary Table S3). The CDRGS was then used as the feature set for consensus clustering of GSE66166 into three molecular subtypes. Immune infiltration was compared between these subtypes, and the two populations that both differed between subtypes and were associated with overall survival, memory B cells and CD8+ T cells, were carried forward as the traits for the module–trait analysis. WGCNA was performed on the CDRGS genes, and 15 hub genes were extracted from the green module (35 genes; Supplementary Table S4). The 15 hub genes are therefore a subset of the CDRGS, and they formed the candidate set for LASSO Cox regression.

Enrichment analysis. Single-sample gene set enrichment analysis (ssGSEA) was implemented using the GSVA R package on the basis of the gene set enrichment approach [21] to quantify the activation levels of specific biological pathways. Hallmark gene signatures were retrieved from the Molecular Signatures Database (MSigDB; https://www.gsea-msigdb.org/gsea/msigdb/), and curated reference gene sets were obtained from the materials of Chung et al. [22].

Consensus clustering for molecular subtyping. To stratify FL patients into distinct molecular subtypes, unsupervised K-means consensus clustering was performed on the CDRGS expression profiles using the ConsensusClusterPlus R package. The optimal cluster number was determined by inspecting the empirical cumulative distribution function (CDF) plots and the consensus matrix. The clustering parameters were as follows: maxK=9, reps=50, pItem=0.8, and pFeature=1 [23].

Tumor microenvironment and immune infiltration analysis. The non-tumor cell fractions of the FL bulk transcriptomes were estimated using the ESTIMATE algorithm (version 1.0.13), which produced StromalScore, ImmuneScore, and ESTIMATEScore values reflecting the relative levels of stromal and immune infiltration in each sample [24]. Additionally, CIBERSORT was applied to the GSE66166 cohort to estimate the relative abundance of 22 distinct immune cell types directly from the bulk gene

expression profiles [25]. ESTIMATE yields an aggregate measure of total immune and stromal content, whereas CIBERSORT yields the relative proportions of individual populations, which are constrained to sum to unity; the two outputs are therefore not directly comparable. The CIBERSORT-derived abundances of memory B cells and CD8+ T cells were used as the external traits in the subsequent module-trait analysis.

Weighted gene co-expression network analysis. A gene co-expression network was constructed from the CDRGS expression profiles in GSE66166 using the WGCNA R package [26]. A soft-thresholding power of 4 was selected to achieve a scale-free topology with an R^2 fit index of 0.9. Initial gene clusters were generated by hierarchical clustering with a minimum module size of 10 genes, yielding 12 preliminary modules (including the unassigned gray module). Modules with highly correlated eigengenes were merged at a cut height of 0.6, resulting in six modules in addition to the unassigned gray module for downstream analysis. Module eigengenes were then correlated with the CIBERSORT-derived abundances of memory B cells and CD8+ T cells, and hub genes were extracted from the module showing the strongest correlation using thresholds of module membership > 0.6 and gene significance > 0.2.

Construction of the prognostic risk model. LASSO Cox regression analysis was performed using the glmnet R package [27] to identify the most informative prognostic genes and address multicollinearity. The optimal penalty parameter (λ) was determined by 10-fold cross-validation. The 15 WGCNA hub genes formed the candidate set, the model was fitted in the 106 GSE66166 patients with complete survival data, and at λ=0.0552 three genes were retained. The expression values of the three model genes were converted to z-scores within each cohort separately, so that risk scores derived from the Illumina and Affymetrix datasets are on a common scale and a single threshold can be applied across cohorts. The resulting risk score was calculated as

$$Risk\ score = (-0.1801 \times SIRPG) + (0.2232 \times FLT3LG) + (-0.0532 \times LAG3).$$

where each term is the z-scored expression value of the gene. Model coefficients and parameters are given in Supplementary Table S5. Patients were stratified into high-risk and low-risk groups using the median risk score as the cutoff. Two threshold strategies were applied. In the primary analysis the median was computed within each cohort. In a prespecified sensitivity analysis the threshold was fixed at the median risk score of the GSE66166 training cohort (0.0062) and applied unchanged to both validation cohorts, with no cohort-specific re- optimization. All measures of discrimination and all Cox models were computed on the continuous risk score and are independent of any threshold. In the Cox models the risk score was entered per standard deviation so that the hazard ratio is interpretable. The

same equation, with the coefficients unchanged, was applied to the independent patient cohort described above, using expression values z-scored within that cohort.

Evaluation of model performance. Discrimination was assessed by time-dependent receiver operating characteristic (ROC) analysis at 1, 3, and 5 years using the timeROC R package with marginal weighting for censoring, and by Harrell's concordance index (C-index) with 95% confidence intervals derived from the standard error of the concordance estimate. Calibration was evaluated using bootstrap-resampled calibration curves (B=500 resamples) generated with the rms R package. Univariable and multivariable Cox proportional hazards regression were used to determine whether the three-gene risk score was prognostic independently of the clinical variables available in each cohort; the proportional hazards assumption was verified using scaled Schoenfeld residuals. For GSE66166, two models were fitted, one adjusting for age, sex, and ECOG performance status and one adjusting for M7-FLIPI. For GSE119214, a single model adjusted for M7-FLIPI and the m-GEP score. For GSE16131, two models were fitted, one adjusting for age > 60 years, Ann Arbor stage > 2, elevated LDH, and extranodal involvement, and one adjusting for the composite IPI score. Clinical usefulness was assessed by decision-curve analysis for 5-year overall survival using the ggDCA R package. Net benefit was computed across threshold probabilities from 0 to 60% for the risk score alone, for the clinical index available in the cohort concerned (M7-FLIPI in GSE66166 and GSE119214, the composite IPI in GSE16131), and for the two combined, with the treat-all and treat-none strategies as references. No formal discrimination or calibration analysis was attempted in the independent patient cohort, whose size does not support it.

Cell culture. Eight human cell lines (Procell Life Science Co., Ltd.) were used in this study. SU-DHL-4, SU-DHL-6, OCI-LY8, SC-1, WSU-FSCCL, RL, and DOHH2 were maintained in RPMI-1640 medium, and Hmy.C1R was maintained in IMDM medium. All media were supplemented with 10% fetal bovine serum and 1% penicillin-streptomycin, and cell cultures were kept in a humidified incubator at 37 °C with 5% CO_2 . The panel was assembled to span the spectrum from indolent FL to transformed disease: SC-1 and WSU-FSCCL are follicular lymphoma-derived lines, and SU-DHL-4, RL, and DOHH2 carry the t(14;18)(q32;q21)/IGH::BCL2 translocation characteristic of FL; DOHH2 was established from a patient whose follicular lymphoma had undergone histological transformation. Because a substantial proportion of FL patients transform to DLBCL, lines representing both ends of this continuum were included. SU-DHL-4 was selected for the *in vivo* tumor model on the basis of its reliable subcutaneous engraftment in preliminary experiments.

***In vivo* tumor xenograft model.** Four-week-old female SCID mice (n=6; Beijing HFK Bioscience Co., Ltd., Beijing, China) were used to establish the subcutaneous xenograft model. Animals were housed

under specific-pathogen-free conditions at 20-26 °C and 40-70% relative humidity on a 12 h light/dark cycle with free access to food and water, and were acclimatized for 7 days before inoculation. SU-DHL-4 cells (5×10^6 per mouse) suspended in phosphate-buffered saline (PBS) were injected into the right flank of each mouse. All animals received the same inoculum and were assigned to a single experimental group; no randomization or group allocation was therefore applicable. Tumor formation and animal health were monitored every 3 days, and tumor dimensions were measured with digital calipers, with volume calculated as length × width²/2. The predefined experimental endpoint was a tumor volume of approximately 1,000 mm³, at which point the animals were euthanized and the subcutaneous tumors were excised and photographed. Humane endpoints, at which animals were euthanized irrespective of tumor volume, comprised ulceration of the tumor, body weight loss exceeding 20% of the pre-inoculation weight, or impaired mobility preventing access to food and water. Immunohistochemical assessment was performed by an assessor blinded to specimen identity. The xenograft experiment was descriptive in intent and no inferential statistical testing was applied to animal-level data. All animal procedures were performed in accordance with institutional guidelines for laboratory animal care and are reported in accordance with the ARRIVE 2.0 guidelines.

Western blot analysis. Total cellular proteins were extracted from the eight cell lines using RIPA lysis buffer, and protein concentrations were measured with a BCA protein assay kit. Equal amounts of protein were separated by sodium dodecyl sulfate-polyacrylamide gel electrophoresis (SDS-PAGE) and transferred onto polyvinylidene fluoride (PVDF) membranes. The membranes were blocked with 5% non-fat milk at room temperature and incubated overnight at 4 °C with primary antibodies against SIRPB2/SIRPG (Novus Biologicals, #NBP2-33512, 1:1000), FLT3LG (Cusabio, #CSB-PA008734LA01HU, 1:1000), LAG3 (Affinity Biosciences, #DF13960, 1:1000), and β-actin (CST, #4967, 1:1000). After washing, the membranes were incubated with the corresponding secondary antibodies. Protein bands were visualized using enhanced chemiluminescence (ECL), and band intensities were quantified using ImageJ software with β-actin as the internal loading control. All primary antibodies were used as validated by the respective commercial vendors.

RNA extraction and quantitative real-time PCR (RT-qPCR). Total RNA was extracted from cultured cell lines and from patient lymph node specimens using TRIzol™ (Thermo Fisher Scientific, #15596018CN). RNA concentration and purity were assessed by spectrophotometry (A260/280=1.8-2.0). Complementary DNA was synthesized from 1 μg of total RNA using the PrimeScript FAST RT Reagent Kit with gDNA Eraser (Takara, #RR092A, Japan) according to the manufacturer's protocol. Reverse transcription quantitative PCR (RT-qPCR) was performed using iTaq™ Universal SYBR® Green Supermix (Bio-Rad, #1725121, USA) on a CFX Connect™ Real-Time PCR Detection System

(Bio-Rad, USA). Each 20 µl reaction contained 10 µl supermix, 500 nM of each primer and 1 µl cDNA. Cycling conditions were 95 °C for 30 s, followed by 40 cycles of 95 °C for 5 s and 60 °C for 30 s. Melting curve analysis was performed after each run to confirm amplification specificity, and no-template controls were included on every plate. Relative mRNA expression of target genes was normalized to GAPDH and calculated using the 2^-ΔCt method; GAPDH was used as the reference gene in both the cell line and the patient tissue experiments. All primers were designed against human transcripts and were identical for the cell line and patient tissue experiments. The primer sequences were as follows: SIRPG: forward 5‘-TCCTCCTGGTCCTTTCCT-3’; reverse: 5‘-GGCTGTCTTTCCAACTGTG-3’; FLT3LG: forward 5‘-GCTGGGTCCAAGATGCAAGG-3’; reverse: 5‘-GGTCTGGACGAAGCGAAGAC-3’; LAG3: forward 5‘-GCGGGGACTTCTCGCTATG-3’; reverse: 5‘-GGCTCTGAGAGATCCTGGGG-3’; GAPDH: forward 5‘-TCCTCTGACTTCAACAGCGA-3’, reverse: 5‘-GGGTCTTACTCCTTGGAGGC-3’.

Immunohistochemistry (IHC). SU-DHL-4 xenograft tumors were excised, fixed in 4% paraformaldehyde and embedded in paraffin. Archival paraffin-embedded diagnostic lymph node specimens from the FL cohort were retrieved and processed in parallel. Sections were deparaffinized, rehydrated and subjected to heat-mediated antigen retrieval in citrate buffer, then incubated overnight at 4 °C with rabbit polyclonal antibodies against SIRPG (Novus Biologicals, #NBP2-33512, 1:50), FLT3LG (Cusabio, #CSB-PA008734LA01HU, 1:500) and LAG3 (Affinity Biosciences, #DF13960, 1:100). Negative controls were processed in parallel with PBS substituted for the primary antibody. All sections were subsequently incubated with an HRP-conjugated secondary antibody and developed with a DAB substrate kit, counterstained with hematoxylin, and imaged by light microscopy. Sections from the patient specimens were reviewed independently by two observers blinded to histological grade and clinical data; staining is reported descriptively and was not scored.

Statistical analysis. All analyses were performed using R version 4.0.2 and GraphPad Prism version 8.0.2. Differences between two groups were assessed using Student's t-test, or the Mann-Whitney U test where the assumption of normality was not met, and comparisons among three or more groups were performed using the non-parametric Kruskal-Walli’s test, with one-way analysis of variance (ANOVA) used where the assumptions of normality and homogeneity of variance were met. Expression in each lymphoma cell line was compared with that in the Hmy.C1R reference line by one-way ANOVA with Dunnett's post hoc test. Pearson and Spearman correlation coefficients were used to evaluate linear and monotonic relationships, respectively. Survival curves were estimated using the Kaplan–Meier method and compared using the log-rank test. A two-sided $p < 0.05$ was considered statistically significant. In the independent patient cohort, transcript levels were compared between two

groups by the Mann-Whitney U test and among three groups by the Kruskal-Walli's test with Dunn's post hoc test; these subgroup analyses were exploratory and the P values are reported unadjusted for multiple comparisons.

Ethics approval and consent to participate. The bioinformatics portion of this study was based on the secondary analysis of publicly available datasets and was therefore exempt from institutional ethics committee approval. All public data were collected in accordance with the ethical guidelines of the respective databases, and the original studies obtained the necessary ethical approvals. The retrospective study of archival diagnostic lymph node specimens from patients with follicular lymphoma was approved by the Institutional Ethics Committee of West China Second University Hospital, Sichuan University (Approval No. 2021-190), which waived the requirement for written informed consent because the study was retrospective and used archived paraffin-embedded tissue; all procedures involving human material were performed in accordance with the Declaration of Helsinki. The animal experiments were approved by the Laboratory Animal Ethical Committee of West China Hospital of Sichuan University (Approval No. 2021-S-012), and all procedures were performed in accordance with institutional guidelines for laboratory animal care and are reported in accordance with the ARRIVE 2.0 guidelines.

Results

The flow chart of this study is shown in Figure 1, and the gene-level filtering cascade underlying the CDRGS and the final model is shown in Supplementary Figure S4.

Identification of cell types in FL by single-cell RNA sequencing. A total of 3,793 cells expressing 18,570 genes were retained for downstream analysis after removing cells with low transcriptomic complexity, weakly expressed genes, and high mitochondrial gene content. Unsupervised graph-based clustering classified all filtered cells into 14 distinct clusters (Figure 2A), and the top marker gene per cluster (ranked by logFC) was visualized (Figures 2B, 2C). A heatmap of the top 10 marker genes per cluster confirmed that these gene signatures could reliably discriminate the clusters (Figure 2D). Cell type annotation was performed against the "ref_Monaco_114s.RData" reference dataset, and the 14 clusters were assigned to 10 cell types, including 3 B cell subtypes (naive, switched memory, and exhausted B cells), 5 T cell subtypes, 1 dendritic cell subtype, and 1 NK cell subtype (Figure 2E).

Characterization of tumor-infiltrating immune cells in FL. To characterize the immune microenvironment, the expression of marker genes for B cells, T cells, macrophages, NK cells, and dendritic cells was assessed across all scRNA-seq samples. ssGSEA showed that B cell-associated markers were enriched in samples FL1B, FL2B, and FL3B, consistent with their sample origin, while T

cell-associated markers were enriched in samples FL1NB, FL2NB, and FL3NB; macrophage-associated markers showed no sample-specific aggregation (Figure 3A). Functional state analysis of B cells identified gene signatures corresponding to anti-apoptotic, pro-apoptotic, naïve memory, cytokine, proliferation, and germinal center phenotypes (Figure 3B). T cells were further subclassified into naïve, costimulatory, regulatory, cytotoxic, exhausted, G1/S, and G2/M populations (Figure 3C). Hallmark gene set ssGSEA further demonstrated that naïve CD4+ and naïve CD8+ T cells were significantly enriched for KRAS signaling, switched memory B cells were inversely correlated with the interferon response, plasmacytoid dendritic cells and NK cells were enriched across multiple hallmark pathways, and the epithelial-mesenchymal transition signature was significantly negatively correlated with exhausted B cells (Supplementary Figure S5).

Pseudotime trajectory analysis identifies three differentiation states of FL cells. To investigate the differentiation potential of FL cell subsets, 1,604 differentially expressed genes between clusters were used as the input feature set (Supplementary Table S2). Cells were ordered along simulated pseudotime trajectories based on transcriptomic similarity (Figure 4A). The distribution of each annotated cell type along the trajectory is shown in Figure 4B, and hierarchical clustering of the ten cell types is shown in Figure 4C. B cell populations, predominantly switched memory B cells, were concentrated in State 1, whereas T cells, NK cells, and dendritic cells were distributed across States 2 and 3, which had the more similar cellular composition (Figure 4D). Differential expression testing across the three states yielded 394 genes, which were designated the CDRGS (Supplementary Table S3).

Molecular subtyping based on CDRGS reveals three FL clusters with distinct prognosis. Based on the expression patterns of CDRGS genes **(**Supplementary Table S3, Supplementary Figure S3), unsupervised K-means consensus clustering was performed on the GSE66166 training cohort. The cumulative distribution function (CDF) curves for k=2-9 are shown in Figure 5A, and k=3 was selected as the optimal number of clusters based on consensus matrix stability (Figure 5B). Differentially expressed genes among the three sample clusters are presented in Figure 5C. Kaplan-Meier survival analysis demonstrated that patients in Cluster C2 had significantly worse prognosis than those in Clusters C1 and C3 (Figure 5D). The Sankey diagram further showed that Cluster C2 was enriched in patients aged > 60 years, with ECOG of 2 or 3, and M7-FLIPI $\geq$ 0.8 (Figure 5E).

Tumor microenvironment and immune infiltration differences among CDRGS clusters. To dissect the clinical relevance of tumor-infiltrating immune cells across the three CDRGS clusters, ESTIMATE scoring and CIBERSORT analysis were performed. ESTIMATEScore, ImmuneScore, StromalScore, and TumorPurity all differed significantly between Clusters C1 and C2 and between Clusters C2 and C3, but not between Clusters C1 and C3 (overall comparison by Kruskal-Wallis's test

with pairwise Wilcoxon rank-sum tests) (Figures 6A-6D). CIBERSORT was applied to deconvolute the relative abundance of 22 immune cell types from the GSE66166 bulk transcriptomic profiles (Figures 6E, 6F). Kaplan-Meier analysis indicated that patients with a high abundance of memory B cells had improved overall survival ($p=0.010$; Figure 6G), whereas patients with low abundance of CD8+ T cells showed longer survival ($p=0.032$; Figure 6H).

These results indicate that the three CDRGS-defined subtypes differ not only in tumor-cell-intrinsic transcription but also in the extent of non-malignant cell infiltration, since the ESTIMATE-derived scores separate Cluster C2, which carried the poorest survival, from Clusters C1 and C3, and the CIBERSORT profiles show that this difference is distributed across multiple immune populations rather than driven by any single cell type. The two analyses are not directly comparable: ImmuneScore is an aggregate measure of total immune content, whereas CIBERSORT estimates the relative proportions of 22 populations that are constrained to sum to unity, so a change in the proportion of one population can occur without any change in total immune infiltration. They are therefore reported as complementary descriptions rather than as independent confirmation of the same conclusion.

WGCNA identifies a co-expression module associated with inferred memory B cell abundance. To further explore the relationship between gene co-expression structure and inferred immune cell composition, WGCNA was performed on the CDRGS genes in the GSE66166 dataset. A scale-free co-expression network was constructed at a soft threshold of $\beta=4$ (Figure 7A), and six co-expression modules, in addition to the unassigned gray module, remained after merging highly correlated modules (Figure 7B). Among them, the green module (35 genes; Supplementary Table S4) showed the strongest correlation with CIBERSORT-inferred memory B cell abundance among all modules ($r=-0.53$, $p=1 \times 10^{-11}$; Figure 7C); the correlation is negative, indicating that higher green-module eigengene values correspond to lower inferred memory B cell abundance. Within the green module, gene significance for memory B cells was highly correlated with module membership ($r=0.84$, $p=2.8 \times 10^{-10}$; Figure 7D), confirming the internal coherence of the module. Fifteen hub genes were extracted from the green module using a module membership threshold of > 0.6 and a gene significance threshold of > 0.2, and included all three genes subsequently retained by LASSO Cox regression.

Construction and evaluation of a three-gene prognostic risk model. GSE66166 was used as the training cohort, while GSE119214 and GSE16131 served as validation cohorts. LASSO Cox regression was applied to address multicollinearity and reduce the number of model genes using the "glmnet" R package, and the coefficient profile along the regularization path is shown in Figure 8A. The optimal λ was determined by 10-fold cross-validation (Figure 8B), giving $\lambda=0.0552$, yielding a three-gene prognostic model comprising *SIRPG*, *FLT3LG*, and *LAG3* with coefficients of -0.1801, 0.2232 and -

0.0532 respectively (Supplementary Table S5). Individual risk scores were calculated for each patient (Figure 8C), and Kaplan-Meier analysis demonstrated that patients in the high-risk group had significantly worse prognosis than those in the low-risk group in the training cohort (p=0.023; Figure 8D). Using cohort-specific medians, high-risk patients had shorter overall survival in GSE119214 (p=0.0066; Figures 8E, 8F), and the separation was in the same direction in GSE16131 without reaching significance (p=0.073; Figures 8G, 8H). In all three cohorts the expression heatmaps show SIRPG and LAG3 decreasing and FLT3LG increasing across the ascending risk-score axis, consistent with the signs of the model coefficients (Figures 8C, 8E, 8G). Because the choice of threshold could affect these comparisons, the analysis was repeated with the threshold fixed at the training-cohort median (0.0062) and applied unchanged to both validation cohorts. Under this fixed threshold, high-risk patients again had shorter overall survival in GSE119214 (p=0.028) and in GSE16131 (p=0.049; Supplementary Figures S6A, S6B). The two threshold strategies therefore gave results in the same direction in both validation cohorts, with the log-rank p value in GSE16131 falling on either side of the conventional significance level (0.073 and 0.049).

Discrimination, calibration, and independence from clinical variables. Time-dependent ROC analysis (Supplementary Figures S6C-S6E) yielded AUCs at 1, 3 and 5 years of 0.779, 0.645 and 0.698 in GSE66166 (C-index 0.672, 95% CI 0.575-0.769) and 0.703, 0.608 and 0.651 in GSE119214 (C-index 0.609, 95% CI 0.526-0.691). Discrimination was lower in GSE16131 (AUCs 0.540, 0.580 and 0.561; C-index 0.544, 95% CI 0.479-0.609). Bootstrap-resampled calibration curves (Supplementary Figures S7A-S7C) approximated the diagonal in GSE66166, deviated at intermediate predicted probabilities in GSE119214, and were comparatively flat in GSE16131. In decision-curve analysis for 5-year overall survival (Supplementary Figures S8A-S8C), the score yielded net benefit over the treat-all and treat-none strategies across threshold probabilities of 15-50% in GSE66166, 15-48% in GSE119214 and 15-30% in GSE16131. Adding the score to M7-FLIPI increased net benefit over M7-FLIPI alone in GSE66166 and GSE119214; in GSE16131 the curve for the score plus IPI was essentially superimposed on that for IPI alone.

Multivariable Cox models were fitted separately in each cohort using the covariates available in that dataset, with the score entered per standard deviation (Supplementary Figure S9A-S9C). The score remained associated with overall survival in GSE66166 after adjustment for age, sex and ECOG performance status (HR 2.28, 95% CI 1.52-3.41, $p < 0.001$) and, in a separate model, for M7-FLIPI (HR 2.31, 95% CI 1.50-3.56, $p < 0.001$), and in GSE119214 after adjustment for M7-FLIPI and the m-GEP score (HR 2.36, 95% CI 1.44-3.88, $p < 0.001$). M7-FLIPI was itself strongly prognostic in both cohorts (HR 5.87 and 4.73, respectively; both $p < 0.001$). In GSE16131 the adjusted estimate was

directionally concordant but did not reach significance (HR 1.30, 95% CI 0.99-1.71, p=0.062), and was further attenuated when the composite IPI replaced its individual components (HR 1.20, 95% CI 0.88-1.63, p=0.241).

Expression of SIRPG, FLT3LG and LAG3 in lymphoma cell lines and xenograft tissue. Baseline expression of the three signature genes was examined in seven lymphoma cell lines (SU-DHL-4, SU-DHL-6, OCI-LY8, SC-1, WSU-FSCCL, RL and DOHH2) and in the non-malignant B lymphoblastoid line Hmy.C1R. Western blotting showed higher LAG3, FLT3LG and SIRPG protein levels in all seven lymphoma lines than in Hmy.C1R (Figure 9A), and densitometric quantification confirmed the difference (Figure 9B). RT-qPCR gave concordant results at the transcript level (Figure 9C).

Immunohistochemistry on tumor tissue from the SU-DHL-4 xenograft model showed densely packed mononuclear cells with high nucleocytoplasmic ratios. All three proteins gave positive chromogenic signal, which was absent in negative-control sections (Figure 9D). SIRPG showed diffuse membranous and cytoplasmic staining that delineated cell boundaries; FLT3LG showed a comparable distribution with granular cytoplasmic staining; LAG3 showed focal membranous staining in clusters of tumor cells.

Association of the three genes with clinicopathological features and outcome in an independent patient cohort. RT-qPCR was performed on diagnostic lymph node specimens from an independent cohort of patients with FL (n=60), and transcript levels were related to histological grade, BCL2/BCL6 rearrangement status, Ann Arbor stage, FL-IPI, end-of-treatment Deauville score and outcome (Figure 10); group sizes are given in each panel. Transcript levels of the three genes did not differ between low- and high-grade FL (p=0.2117, 0.2554 and 0.2458 for SIRPG, FLT3LG and LAG3) or between cases with and without the rearrangements assessed (p=0.2814, 0.6524 and 0.5522), and SIRPG did not vary significantly across any clinical variable examined (Figures 10D-10F). Three comparisons reached nominal significance, each in the direction predicted by the sign of the corresponding model coefficient: LAG3 declined across increasing FL-IPI categories (p=0.0122) and increasing Deauville scores (p=0.0420), and FLT3LG rose with increasing Deauville score (p=0.0273). SIRPG declined across FL-IPI categories (p=0.0741) and FLT3LG rose across Ann Arbor stage (p=0.0704) without reaching significance. These analyses were exploratory and unadjusted for multiple comparisons.

Patients were dichotomized at the median transcript level of each gene for survival analysis. Event-free survival was shorter in the high-FLT3LG group (p=0.0122; Figure 10B), longer in the high-SIRPG group without reaching conventional significance (p=0.0713; Figure 10A), and unrelated to LAG3 expression (p=0.5768; Figure 10C). The direction of all three associations was concordant with the sign of the corresponding coefficient in the GSE66166 model.

The three-gene risk score was computed in the 24 patients with complete expression data for all three genes using the GSE66166 coefficients (Figure 10G). SIRPG and LAG3 expression fell and FLT3LG rose across the ascending risk-score axis, and events clustered in the high-risk half of the ranking; the difference in event-free survival between risk groups was not significant (p=0.3696; Figure 10H). Immunohistochemistry on sections from the same archive showed all three proteins in routine diagnostic material, with SIRPG and LAG3 staining more intense in low-grade and FLT3LG in high-grade cases (Figure 10I); staining was assessed descriptively and was not scored.

Discussion

Follicular lymphoma is an incurable B-cell malignancy characterized by a heterogeneous clinical course and a persistent risk of histological transformation to aggressive lymphoma [28-31]. Next-generation sequencing has defined the genomic landscape of FL [32-34], and single-cell sequencing has extended this to transcriptional profiling at single-cell resolution, providing a means of dissecting the spatial and temporal components of intratumoral heterogeneity [35-37]. Malignant FL cells depend heavily on the tumor microenvironment for survival and proliferation [38], and the gene expression profiles of tumor-infiltrating immune cells have been linked to clinical outcome [39]: a high content of PD-1+ tumor-infiltrating lymphocytes has been associated with improved overall survival in FL [40], the composition of tumor cell states and immune ecosystems has been linked to outcome in aggressive B-cell lymphoma [41], regulatory T cells have been associated with poor overall survival and increased risk of transformation [42], tumor-associated macrophages predict an unfavorable clinical course [43], and follicular lymphoma cells induce dysfunction of the T cell immunological synapse [44] together with changes in CD4+ and CD8+ T cell gene expression [45] that bear on both overall survival and time to transformation [46-48]. Because differentiation programs are themselves tightly linked to malignant transformation and disease progression, and redirecting malignant cells toward a more differentiated and less aggressive state has been explored therapeutically in several cancers [49], we screened genes defined by the differentiation states of FL cells at single-cell resolution.

In this study, scRNA-seq resolved 3,793 FL cells into 14 clusters and 10 annotated cell types. Pseudotime analysis ordered these cells into three differentiation states, and differential expression across the states defined a 394-gene cell differentiation-related gene set (CDRGS). Consensus clustering of the GSE66166 training cohort on the CDRGS separated three molecular subtypes with distinct survival, and ESTIMATE and CIBERSORT showed that these subtypes differ in the extent and composition of non-malignant infiltration rather than in tumor-cell-intrinsic transcription alone. WGCNA identified a green module whose eigengene was, among all modules, the most strongly

correlated with the inferred abundance of memory B cells, and LASSO Cox regression retained SIRPG, FLT3LG and LAG3 from its hub genes. The complete gene-level filtering cascade, with the number of genes retained at each step and the criteria applied, is shown in Supplementary Figure S4.

Among the three model genes, SIRPG encodes an immunoglobulin-like cell surface receptor that binds CD47 and mediates cell–cell adhesion [50]; it also enhances activation-induced T cell proliferation, an effect that has recently been shown to be CD47-independent [51]. In a previous FL cohort, an immune biomarker pattern that included loss of intrafollicular CD8 and PD-1 expression together with intrafollicular SIRPα expression was correlated with the risk of early treatment failure [46]. FLT3LG, the ligand of FMS-related receptor tyrosine kinase 3, sustains the dendritic cell compartment and thereby shapes antitumor immunity [52], has been incorporated into a 10-gene CD8+ T cell differentiation signature that may predict prognosis in FL patients treated with rituximab–bendamustine [47]. LAG3 is predominantly expressed on PD-1+ and TIM-3+ T cells, where constitutive expression marks the transition from a partially functional to an exhausted state [53]; in follicular lymphoma specifically, LAG3 expression defines exhaustion of intratumoral PD-1+ T cells and has been correlated with poor outcome [54]. Their expression in bulk tissue is therefore expected to track the size of a T cell compartment that has been associated with more favorable outcome in FL [8-11, 48]. The cell line and xenograft experiments establish a narrower point, namely that the malignant B cells themselves also transcribe and translate all three genes; they do not indicate which compartment dominates the measurement in a heterogeneous tumor, and we therefore do not present them as support for the direction of the coefficients.

The independent patient cohort provides an external check on the individual genes (Figure 10). Each gene's association with outcome followed the sign of its coefficient: high FLT3LG expression was associated with markedly shorter event-free survival, high SIRPG expression with longer event-free survival at the margin of significance, and LAG3 with neither. The associations with established clinical indices pointed the same way, LAG3 declining across increasing FL-IPI and Deauville categories and FLT3LG rising with increasing Deauville score, and the immunohistochemical staining showed the same directional contrast between low-grade and high-grade disease, although the corresponding transcript-level comparison across histological grade was not significant. Because these specimens were not used at any stage of model derivation, the associations are independent of it. They are nevertheless exploratory: most comparisons were not significant, the endpoint is event-free survival rather than the overall survival used in the public datasets, follow-up is short, and the cohort is too small for the composite score to be tested against a time-to-event endpoint.

Two of the microenvironmental findings require a cautious reading. Memory B cells can re-enter the germinal center under permissive conditions, a property that has been proposed to sustain recurrent lymphomagenesis in FL [55, 56], which makes their inferred abundance a plausible correlate of the differentiation axis captured by the CDRGS. In our data the green module eigengene was negatively correlated with the CIBERSORT-inferred abundance of memory B cells ($r=-0.53$, $p=1 \times 10^{-11}$), so that higher eigengene values correspond to lower inferred memory B cell abundance; since higher inferred abundance was associated with better overall survival in GSE66166, genes drawn from this module track the less favorable end of the same axis. This coherence should not be overstated, since WGCNA identifies co-expressed genes rather than cell populations, the abundances were inferred by deconvolution rather than measured directly, and the relationship is a correlation within a single cohort. The second finding is that the association of lower inferred CD8+ T cell abundance with longer overall survival (Figure 6H) is counterintuitive relative to the paradigm established in solid tumors and to reports that CD8+ T cell content in diagnostic lymph nodes is a favorable prognostic factor in FL [48]. Deconvolution does not resolve functional state, and intratumoral CD8+ T cells in FL frequently co-express PD-1, TIM-3 and LAG3 and are functionally impaired [54], so a high inferred CD8+ fraction may reflect an exhausted rather than a protective compartment; CIBERSORT fractions are also constrained to sum to unity, so samples of lower malignant cell content yield higher apparent immune fractions, and TumorPurity differed across the CDRGS clusters (Figure 6D). We therefore present this finding as hypothesis-generating, requiring confirmation by methods that resolve functional state and spatial context.

Discrimination was modest and varied across cohorts. Concordance indices of 0.672 in GSE66166 and 0.609 in GSE119214, with time-dependent areas under the curve at 1, 3 and 5 years between 0.61 and 0.78, are informative at the group level but not sufficient for individual prediction, and in GSE16131 discrimination was close to chance (C-index 0.544) with correspondingly flat calibration (Supplementary Figure S8). In multivariable models (Supplementary Figure S9) the score remained associated with overall survival in GSE66166 after adjustment for age, sex and ECOG status and, in a separate model, alongside M7-FLIPI, and in GSE119214 after adjustment for M7-FLIPI and the m-GEP score, with closely comparable effect sizes per standard deviation (HR 2.28, 2.31 and 2.36); M7-FLIPI was itself the stronger predictor (HR 5.87 and 4.73). In GSE16131 the adjusted hazard ratio lay in the same direction but did not reach significance, and the score was no longer associated with survival once the composite IPI replaced its individual components; decision-curve analysis followed the same pattern (Supplementary Figure S7). Profiling on a different array platform, treatment in an earlier era and sparser annotation are plausible contributors to the attenuated signal in that cohort.

Several FL prognostic signatures have been derived from bulk transcriptomic data alone; the present model differs in that its candidate gene set was defined in single-cell differentiation states, was interpreted against the composition of the microenvironment, and had its constituent genes examined in lymphoma cell lines, in a xenograft and in patient diagnostic material.

Several limitations should be acknowledged. First, the cell line and xenograft experiments show that the three genes are transcribed, translated and detectable in situ, and thus that the malignant cells express them; they do not constitute prognostic validation, which was performed at the patient-cohort level in GSE66166, GSE119214 and GSE16131 and, for the individual genes, in the independent cohort. Second, of the seven lymphoma lines, SC-1 and WSU-FSCCL are of follicular lymphoma origin and DOHH2 derives from a patient with transformed FL, whereas SU-DHL-4, the line used for the xenograft, is a t(14;18)-positive germinal center B-cell DLBCL line selected for its reliable engraftment; the immunodeficient SCID host also lacks the T cell compartment that the signature appears to reflect, so the *in vivo* work should be read as evidence of protein expression in lymphoma tissue rather than as a model of FL microenvironmental biology. Third, the independent cohort is small and retrospective, follow-up is short, and its subgroup comparisons were exploratory and unadjusted for multiplicity. Finally, the public cohorts differ in clinical annotation (Supplementary Table S1), neither treatment regimen nor transformation status was recorded in any of them, and because expression values were standardized within each dataset the threshold is relative to the cohort in which it is applied rather than an absolute cut-point.

Overall, this study derived a cell differentiation-related gene set from single-cell data in FL and used it to construct a three-gene risk score that was associated with overall survival in the training cohort and in GSE119214, showed a directionally concordant but non-significant association in GSE16131, and carried prognostic information not accounted for by M7-FLIPI in the two cohorts in which that index was available. In an independent patient cohort, each gene's association with outcome and with established clinical indices followed the direction predicted by its coefficient. Discrimination was nevertheless modest and was not reproduced on the older array platform, so the score is at present a candidate for risk stratification at the group level rather than a tool for individual prediction. Functional studies using knockdown and overexpression in FL-derived lines, models retaining a human immune compartment, direct quantification of immune populations by multiplex immunohistochemistry or spatial transcriptomics, and prospective validation with formal nested-model comparison against M7-FLIPI would be the appropriate next steps.

Acknowledgements: All datasets analyzed in this study are publicly available from the Gene Expression Omnibus (GEO) database (https://www.ncbi.nlm.nih.gov/geo/) under the accession numbers GSE182434, GSE66166, GSE119214, and GSE16131.

This research was funded by 1·3·5 projects for disciplines of excellence–Clinical Research Incubation Project, West China Hospital, Sichuan University (No: 2019HXFH035). The funders had no role in study design, data collection and analysis, decision to publish, or preparation of the manuscript. The study further received institutional support from Sichuan University: the diagnostic lymph node specimens and the linked clinical records were collected at West China Second University Hospital, and the cell culture, xenograft and immunohistochemistry experiments were carried out at the Institute of Critical Care Medicine, West China Hospital.

Declaration on the use of artificial intelligence: The authors used a large language model, Claude (Anthropic; Opus5), to improve the language, readability and internal consistency of human-written text. The tool was not used to generate, analyze or interpret any data, to produce any figure, or to formulate the scientific conclusions. All text suggested by the tool was reviewed, verified and, where necessary, rewritten by the authors, who take full responsibility for the content and integrity of the work.

Supplementary data are available in the online version of the paper.

References

[1] KALASHNIKOV I, REUNAMO T, TANSKANEN T, VIISANEN L, MALILA N et al. Transformation and causes of death in follicular lymphoma: A Finnish nationwide population-based study. Br J Haematol 2025; 207: 2417-2425. https://doi.org/10.1111/bjh.70181

[2] KURZ KS, KALMBACH S, OTT M, STAIGER AM, OTT G et al. Follicular Lymphoma in the 5th Edition of the WHO-Classification of Haematolymphoid Neoplasms-Updated Classification and New Biological Data. Cancers 2023; 15: 785. https://doi.org/10.3390/cancers15030785

[3] ENEMARK MH, HEMMINGSEN JK, JENSEN ML, KRIDEL R, LUDVIGSEN M. Molecular Biomarkers in Prediction of High-Grade Transformation and Outcome in Patients with Follicular Lymphoma: A Comprehensive Systemic Review. Int J Mol Sci 2024; 25. https://doi.org/10.3390/ijms252011179

[4] HAN G, DENG Q, MARQUES-PIUBELLI ML, DAI E, DANG M et al. Follicular Lymphoma Microenvironment Characteristics Associated with Tumor Cell Mutations and MHC Class II Expression. Blood cancer discovery 2022; 3: 428-443. https://doi.org/10.1158/2643-3230.Bcd-21-0075

[5] LAURENT C, DIETRICH S, TARTE K. Cell cross talk within the lymphoma tumor microenvironment: follicular lymphoma as a paradigm. Blood 2024; 143: 1080-1090. https://doi.org/10.1182/blood.2023021000

[6] CASULO C, BURACK WR, FRIEDBERG JW. Transformed follicular non-Hodgkin lymphoma. Blood 2015; 125: 40-47. https://doi.org/10.1182/blood-2014-04-516815
[7] OKOSUN J, BÖDÖR C, WANG J, ARAF S, YANG CY et al. Integrated genomic analysis identifies recurrent mutations and evolution patterns driving the initiation and progression of follicular lymphoma. Nat Genet 2014; 46: 176-181. https://doi.org/10.1038/ng.2856
[8] RADE M, BÖHLEN S, NEUHAUS V, LÖFFLER D, BLUMERT C et al. A time-resolved meta-analysis of consensus gene expression profiles during human T-cell activation. Genome Biol 2023; 24: 287. https://doi.org/10.1186/s13059-023-03120-7
[9] AMADOR C, BOUSKA A, WRIGHT G, WEISENBURGER DD, FELDMAN AL et al. Gene Expression Signatures for the Accurate Diagnosis of Peripheral T-Cell Lymphoma Entities in the Routine Clinical Practice. J Clin Oncol 2022; 40: 4261-4275. https://doi.org/10.1200/jco.21.02707
[10] TUMEDEI MM, PICCININI F, AZZALI I, PIRINI F, BRAVACCINI S et al. Follicular Lymphoma Microenvironment Traits Associated with Event-Free Survival. Int J Mol Sci 2023; 24. https://doi.org/10.3390/ijms24129909
[11] TAMMA R, INGRAVALLO G, ANNESE T, GAUDIO F, PERRONE T et al. Tumor Microenvironment and Microvascular Density in Follicular Lymphoma. J Clin Med 2022; 11: 1257. https://doi.org/10.3390/jcm11051257
[12] SHAIN KH, DALTON WS, TAO J. The tumor microenvironment shapes hallmarks of mature B-cell malignancies. Oncogene 2015; 34: 4673-4682. https://doi.org/10.1038/onc.2014.403
[13] YANG ZZ, ANSELL SM. The tumor microenvironment in follicular lymphoma. Clin Adv Hematol Oncol 2012; 10: 810-818.
[14] PASTORE A, JURINOVIC V, KRIDEL R, HOSTER E, STAIGER AM et al. Integration of gene mutations in risk prognostication for patients receiving first-line immunochemotherapy for follicular lymphoma: a retrospective analysis of a prospective clinical trial and validation in a population-based registry. Lancet Oncol 2015; 16: 1111-1122. https://doi.org/10.1016/s1470-2045(15)00169-2
[15] SILVA A, BASSIM S, SARKOZY C, MOTTOK A, LACKRAJ T et al. Convergence of risk prediction models in follicular lymphoma. Haematologica 2019; 104: e252-e255. https://doi.org/10.3324/haematol.2018.209031
[16] ANDOR N, SIMONDS EF, CZERWINSKI DK, CHEN J, GRIMES SM et al. Single-cell RNA-Seq of follicular lymphoma reveals malignant B-cell types and coexpression of T-cell immune checkpoints. Blood 2019; 133: 1119-1129. https://doi.org/10.1182/blood-2018-08-862292
[17] ROIDER T, SEUFERT J, UVAROVSKII A, FRAUHAMMER F, BORDAS M et al. Dissecting intratumour heterogeneity of nodal B-cell lymphomas at the transcriptional, genetic and drug-response levels. Nat Cell Biol 2020; 22: 896-906. https://doi.org/10.1038/s41556-020-0532-x
[18] LIANG L, YU J, LI J, LI N, LIU J et al. Integration of scRNA-Seq and Bulk RNA-Seq to Analyse the Heterogeneity of Ovarian Cancer Immune Cells and Establish a Molecular Risk Model. Front Oncol 2021; 11: 711020. https://doi.org/10.3389/fonc.2021.711020
[19] MULÈ MP, MARTINS AJ, TSANG JS. Normalizing and denoising protein expression data from droplet-based single cell profiling. Nat Commun 2022; 13: 2099. https://doi.org/10.1038/s41467-022-29356-8
[20] TRAPNELL C, CACCHIARELLI D, GRIMSBY J, POKHAREL P, LI S et al. The dynamics and regulators of cell fate decisions are revealed by pseudotemporal ordering of single cells. Nat Biotechnol 2014; 32: 381-386. https://doi.org/10.1038/nbt.2859
[21] SUBRAMANIAN A, TAMAYO P, MOOTHA VK, MUKHERJEE S, EBERT BL et al. Gene set enrichment analysis: a knowledge-based approach for interpreting genome-wide expression profiles. Proc Natl Acad Sci U S A 2005; 102: 15545-15550. https://doi.org/10.1073/pnas.0506580102

[22] CHUNG W, EUM HH, LEE HO, LEE KM, LEE HB et al. Single-cell RNA-seq enables comprehensive tumour and immune cell profiling in primary breast cancer. Nat Commun 2017; 8: 15081. https://doi.org/10.1038/ncomms15081
[23] WILKERSON MD, HAYES DN. ConsensusClusterPlus: a class discovery tool with confidence assessments and item tracking. Bioinformatics 2010; 26: 1572-1573. https://doi.org/10.1093/bioinformatics/btq170
[24] YOSHIHARA K, SHAHMORADGOLI M, MARTÍNEZ E, VEGESNA R, KIM H et al. Inferring tumour purity and stromal and immune cell admixture from expression data. Nat Commun 2013; 4: 2612. https://doi.org/10.1038/ncomms3612
[25] NEWMAN AM, LIU CL, GREEN MR, GENTLES AJ, FENG W et al. Robust enumeration of cell subsets from tissue expression profiles. Nat Methods 2015; 12: 453-457. https://doi.org/10.1038/nmeth.3337
[26] LANGFELDER P, HORVATH S. WGCNA: an R package for weighted correlation network analysis. BMC Bioinf 2008; 9: 559. https://doi.org/10.1186/1471-2105-9-559
[27] FRIEDMAN J, HASTIE T, TIBSHIRANI R. Regularization Paths for Generalized Linear Models via Coordinate Descent. J Stat Softw 2010; 33: 1-22.
[28] LI X, LI N, LIU Y, AN L. Unraveling the complexity of follicular lymphoma: insights and innovations. Am J Cancer Res 2024; 14: 5573-5597. https://doi.org/10.62347/mfug2190
[29] PATIL S, RAJPUT S, PATIL S, MHAISKAR A. B-cell lymphoma: Advances in pathogenesis, diagnosis, and targeted therapies. Pathol Res Pract 2025; 271: 156036. https://doi.org/10.1016/j.prp.2025.156036
[30] JAFFE ES, CARBONE A. Evolution in the Definition of Follicular Lymphoma and Diffuse Large B-Cell Lymphoma: A Model for the Future of Personalized Medicine. Hemato 2022; 3: 466-474. https://doi.org/10.3390/hemato3030032
[31] ARAUJO-AYALA F, BÉGUELIN W. Biology as vulnerability in follicular lymphoma: genetics, epigenetics, and immunogenetics. Blood 2025; 146: 1759-1769. https://doi.org/10.1182/blood.2024026020
[32] MOZAS P, LÓPEZ C, GRAU M, NADEU F, CLOT G et al. Genomic landscape of follicular lymphoma across a wide spectrum of clinical behaviors. Hematological oncology 2023; 41: 631-643. https://doi.org/10.1002/hon.3132
[33] SHELTON V, DETROJA R, LIU T, ISAEV K, SILVA A et al. Identification of genetic subtypes in follicular lymphoma. Blood Cancer J 2024; 14: 128. https://doi.org/10.1038/s41408-024-01111-w
[34] LÓPEZ C, MOZAS P, LÓPEZ-GUILLERMO A, BEÀ S. Molecular Pathogenesis of Follicular Lymphoma: From Genetics to Clinical Practice. Hemato 2022; 3: 595-614. https://doi.org/10.3390/hemato3040041
[35] HU Y, SHEN F, YANG X, HAN T, LONG Z et al. Single-cell sequencing technology applied to epigenetics for the study of tumor heterogeneity. Clin Epigenetics 2023; 15: 161. https://doi.org/10.1186/s13148-023-01574-x
[36] JIA Q, WANG A, YUAN Y, ZHU B, LONG H. Heterogeneity of the tumor immune microenvironment and its clinical relevance. Exp Hematol Oncol 2022; 11: 24. https://doi.org/10.1186/s40164-022-00277-y
[37] RADTKE AJ, ROSCHEWSKI M. The follicular lymphoma tumor microenvironment at single-cell and spatial resolution. Blood 2024; 143: 1069-1079. https://doi.org/10.1182/blood.2023020999
[38] ARNER EN, RATHMELL JC. Metabolic programming and immune suppression in the tumor microenvironment. Cancer Cell 2023; 41: 421-433. https://doi.org/10.1016/j.ccell.2023.01.009

[39] BRUMMEL K, EERKENS AL, DE BRUYN M, NIJMAN HW. Tumour-infiltrating lymphocytes: from prognosis to treatment selection. Br J Cancer 2023; 128: 451-458. https://doi.org/10.1038/s41416-022-02119-4

[40] CARRERAS J, LOPEZ-GUILLERMO A, RONCADOR G, VILLAMOR N, COLOMO L et al. High numbers of tumor-infiltrating programmed cell death 1-positive regulatory lymphocytes are associated with improved overall survival in follicular lymphoma. J Clin Oncol 2009; 27: 1470-1476. https://doi.org/10.1200/jco.2008.18.0513

[41] STEEN CB, LUCA BA, ESFAHANI MS, AZIZI A, SWORDER BJ et al. The landscape of tumor cell states and ecosystems in diffuse large B cell lymphoma. Cancer cell 2021; 39: 1422-37.e10. https://doi.org/10.1016/j.ccell.2021.08.011

[42] FARINHA P, AL-TOURAH A, GILL K, KLASA R, CONNORS JM et al. The architectural pattern of FOXP3-positive T cells in follicular lymphoma is an independent predictor of survival and histologic transformation. Blood 2010; 115: 289-295. https://doi.org/10.1182/blood-2009-07-235598

[43] PITTET MJ, MICHIELIN O, MIGLIORINI D. Clinical relevance of tumour-associated macrophages. Nat Rev Clin Oncol 2022; 19: 402-421. https://doi.org/10.1038/s41571-022-00620-6

[44] RAMSAY AG, CLEAR AJ, KELLY G, FATAH R, MATTHEWS J et al. Follicular lymphoma cells induce T-cell immunologic synapse dysfunction that can be repaired with lenalidomide: implications for the tumor microenvironment and immunotherapy. Blood 2009; 114: 4713-4720. https://doi.org/10.1182/blood-2009-04-217687

[45] KIAII S, CLEAR AJ, RAMSAY AG, DAVIES D, SANGARALINGAM A et al. Follicular lymphoma cells induce changes in T-cell gene expression and function: potential impact on survival and risk of transformation. J Clin Oncol 2013; 31: 2654-2661. https://doi.org/10.1200/jco.2012.44.2137

[46] MONDELLO P, FAMA A, LARSON MC, FELDMAN AL, VILLASBOAS JC et al. Lack of intrafollicular memory CD4 + T cells is predictive of early clinical failure in newly diagnosed follicular lymphoma. Blood Cancer J 2021; 11: 130. https://doi.org/10.1038/s41408-021-00521-4

[47] RAI S, INOUE H, SAKAI K, HANAMOTO H, MATSUDA M et al. Decreased expression of T-cell-associated immune markers predicts poor prognosis in patients with follicular lymphoma. Cancer Sci 2022; 113: 660-673. https://doi.org/10.1111/cas.15224

[48] WAHLIN BE, SANDER B, CHRISTENSSON B, KIMBY E. CD8+ T-cell content in diagnostic lymph nodes measured by flow cytometry is a predictor of survival in follicular lymphoma. Clin Cancer Res 2007; 13: 388-397. https://doi.org/10.1158/1078-0432.CCR-06-1734

[49] ZHU K, XIA Y, TIAN X, HE Y, ZHOU J et al. Characterization and therapeutic perspectives of differentiation-inducing therapy in malignant tumors. Front Genet 2023; 14: 1271381. https://doi.org/10.3389/fgene.2023.1271381

[50] KAUR S, ISENBERG JS, ROBERTS DD. CD47 (Cluster of Differentiation 47). Atlas Genet Cytogenet Oncol Haematol 2021; 25: 83-102. https://doi.org/10.1007/978-3-642-54596-2_200215

[51] MARGUERIE F, SAIFI MA, GEARY B, BARNES D, LIM L et al. Enhancement of activation-induced T cell proliferation by SIRPG in a CD47-independent manner. Front Immunol 2025; 16: 1668361. https://doi.org/10.3389/fimmu.2025.1668361

[52] RÉGNIER P, BANSARD A, CAGNARD N, PODSYPANINA K, DARRASSE-JÈZE G. FLT3L-dependent dendritic cells control tumor immunity by modulating Treg and NK cell homeostasis. Cell Rep Med 2023; 4: 101256. https://doi.org/10.1016/j.xcrm.2023.101256

[53] MARTÍNEZ-PÉREZ A, GRANDA-DÍAZ R, AGUILAR-GARCÍA C, SORDO-BAHAMONDE C, GONZALEZ S. Deciphering LAG-3: unveiling molecular mechanisms and clinical advancements. Biomarker Res 2024; 12: 126. https://doi.org/10.1186/s40364-024-00671-0

[54] YANG ZZ, KIM HJ, VILLASBOAS JC, CHEN YP, PRICE-TROSKA T et al. Expression of LAG-3 defines exhaustion of intratumoral PD-1 + T cells and correlates with poor outcome in follicular lymphoma. Oncotarget 2017; 8. https://doi.org/10.1002/hon.2438_128

[55] SUNGALEE S, MAMESSIER E, MORGADO E, GRÉGOIRE E, BROHAWN PZ et al. Germinal center reentries of BCL2-overexpressing B cells drive follicular lymphoma progression. J Clin Invest 2014; 124: 5337-5351. https://doi.org/10.1172/jci72415

[56] SWAMINATHAN S, MÜSCHEN M. Follicular lymphoma: too many reminders for a memory B cell. J Clin Invest 2014; 124: 5095-5098. https://doi.org/10.1172/jci79189

[57] LEICH E, SALAVERRIA I, BEA S, ZETTL A, WRIGHT G et al. Follicular lymphomas with and without translocation t(14;18) differ in gene expression profiles and genetic alterations. Blood 2009; 114: 826-834. https://doi.org/10.1182/blood-2009-01-198580

Figures

Figure 1. Workflow of the study.

Figure 2. Identification of cell subpopulations in FL by single-cell RNA sequencing. A) t-SNE visualization of 3,793 FL cells classified into 14 clusters; each dot represents a single cell and is colored by cluster identity. B) Violin plots showing the expression of the top marker gene per cluster ranked by logFC. C) Expression patterns of the top marker gene per cluster projected onto the t-SNE plot; red indicates high expression and green indicates low or absent expression. D) Heatmap of the top 10 marker genes per cluster (ranked by logFC). E) t-SNE plot annotated with cell type identities based on the "ref_Monaco_114s.RData" reference dataset.

Figure 3. Single-sample gene set enrichment analysis (ssGSEA) of tumor-infiltrating immune cells in FL, performed with the GSVA R package. A) Heatmap of ssGSEA enrichment scores for B cell, T cell, macrophage, and other immune cell signatures across scRNA-seq samples; B cell- and T cell-related signatures showed the strongest sample-specific aggregation. The lower panel shows the leading-edge genes from the gene sets above. B) Clustering of B cells based on ssGSEA enrichment scores for gene sets representing anti-apoptosis, naïve memory, cytokines, pro-apoptosis, proliferation, and germinal center phenotypes. The lower panel shows the leading-edge genes from each gene set. C) Clustering of T cells based on ssGSEA enrichment scores for gene sets representing naïve, costimulatory, regulatory, cytotoxic, exhausted, G1/S, and G2/M states. The lower panel shows the leading-edge genes from each gene set. GSVA: gene set variation analysis.

Figure 4. Pseudotime trajectory analysis of FL cell subpopulations. A) Cell ordering along the pseudotime trajectory in the two-dimensional reduced space defined by Monocle 2; the three panels are colored by pseudotime, Seurat cluster, and inferred cell state, respectively. B) Distribution of each annotated cell type along the pseudotime trajectory. C) Hierarchical clustering of the 10 annotated cell types based on their distribution across the three inferred states. D) Stacked bar chart showing the proportion of each cell type within each of the three pseudotime states; the dendrogram at the left groups the three states by cellular composition.

Figure 5. Molecular subtyping of FL based on the cell differentiation-related gene signature (CDRGS). A) Cumulative distribution function (CDF) curves of the consensus matrix for k=2 to 9. B) Consensus

matrix at k=3. C) Heatmap of differentially expressed genes among the three molecular subtypes (C1, C2, and C3). D) Kaplan-Meier survival analysis showing that FL patients in cluster C2 had unfavorable overall survival; comparison by log-rank test. E) Sankey diagram showing the distribution of age, sex, ECOG, and M7-FLIPI across the three clusters. CDF: cumulative distribution function; ECOG: Eastern Cooperative Oncology Group performance status; M7-FLIPI: clinicogenetic risk model for follicular lymphoma.

Figure 6. Tumor microenvironment and immune cell infiltration across the three CDRGS clusters. A-D) Violin plots showing the distribution of ESTIMATEScore (A), ImmuneScore (B), StromalScore (C), and TumorPurity (D) across the three clusters; overall comparison by Kruskal-Wallis's test, with pairwise comparisons by Wilcoxon rank-sum test. E) Stacked bar chart showing the relative proportions of 22 immune cell types in each FL sample, estimated by CIBERSORT. F) Box plots showing the fractions of the 22 immune cell types across the three clusters; comparisons by Kruskal-Wallis's test. G) Kaplan-Meier survival analysis stratified by memory B cell abundance (dichotomized at the cohort median; p=0.010, log-rank test). H) Kaplan-Meier survival analysis stratified by CD8+ T cell abundance (dichotomized at the cohort median; p=0.032 log-rank test). *p < 0.05, **p < 0.01, ***p < 0.001; ns: not significant

Figure 7. Identification of hub genes by weighted gene co-expression network analysis (WGCNA). A) Determination of the soft-thresholding power based on the scale-free topology model fit (left) and mean connectivity (right). B) Gene dendrogram and module assignment after dynamic tree cutting; six modules were identified (black, pink, blue, greenyellow, green and yellow), with genes not assigned to any module shown in gray. C) Heatmap of correlations between module eigengenes and the abundance of memory B cells and $CD8^+$ T cells; the green module showed the strongest correlation with memory B cell abundance (r=-0.53, $p=1.0 \times 10^{-11}$). D) Scatter plot of gene significance for memory B cells against module membership within the green module (r=0.84, $p=2.8 \times 10^{-10}$); red dots denote hub genes meeting the criteria of module membership > 0.6 and gene significance > 0.2, including SIRPG, FLT3LG and LAG3.

Figure 8. Construction and validation of the three-gene CDRGS prognostic risk model. A) LASSO coefficient profiles of candidate variables along the regularization path; x-axis, log λ; y-axis, regression coefficients. B) Selection of the optimal λ by 10-fold cross-validation; vertical dashed lines indicate the minimum mean cross-validated error and the one-standard-error criterion. C) Risk score distribution,

survival status and expression heatmap of SIRPG, FLT3LG and LAG3 in the GSE66166 training cohort, ranked by ascending risk score; in the heatmap, orange denotes higher and blue lower z-scored expression. D) Kaplan-Meier analysis of the high- and low-risk groups in the GSE66166 training cohort. E, F) Risk score distribution, survival status and expression heatmap (E) and Kaplan-Meier analysis (F) in the GSE119214 validation cohort. G, H) The corresponding analyses in the GSE16131 validation cohort. In D, F and H, groups were defined by the cohort-specific median risk score and compared by log-rank test. CDRGS, cell differentiation-related gene signature; LASSO, least absolute shrinkage and selection operator.

Figure 9. Expression of SIRPG, FLT3LG and LAG3 in lymphoma cell lines and xenograft tissue. A) Western blot of SIRPG, FLT3LG and LAG3 in seven lymphoma cell lines (SU-DHL-4, SU-DHL-6, OCI-LY8, SC-1, WSU-FSCCL, RL and DOHH2) and in the non-malignant B lymphoblastoid cell line Hmy.C1R; β-actin served as loading control. B) Densitometric quantification of the blots in A using ImageJ, expressed relative to β-actin. C) RT-qPCR analysis of relative SIRPG, FLT3LG and LAG3 mRNA expression in the same eight cell lines, normalized to GAPDH. Data are from three independent experiments (mean±SD); each lymphoma cell line was compared with Hmy.C1R by one-way ANOVA with Dunnett's post hoc test. *$p < 0.05$, **$p < 0.01$, ***$p < 0.001$, ****$p < 0.0001$. D) Representative immunohistochemical staining of SIRPG, FLT3LG and LAG3 in SU-DHL-4 xenograft tumor sections (upper three rows) and the corresponding negative-control sections, in which PBS was substituted for the primary antibody (lower row). Scale bars, 100 μm.

Figure 10. Association of SIRPG, FLT3LG and LAG3 with clinicopathological features and outcome in an independent cohort of patients with follicular lymphoma. A-C) Kaplan-Meier analysis of event-free survival in patients dichotomized at the cohort median transcript level of SIRPG (A), FLT3LG (B) and LAG3 (C); group sizes are shown in each panel and comparisons were made by log-rank test. D–F) Relative mRNA expression (2^−ΔCt, normalized to GAPDH) of SIRPG (D), FLT3LG (E) and LAG3 (F) across histological grade, BCL2 and BCL6 rearrangement status, Ann Arbor stage, FL-IPI and end-of-treatment Deauville score. Each circle represents one patient; bars show the median and interquartile range; group sizes and exact P values are given in each panel. Two-group comparisons were made by the Mann-Whitney U test and comparisons across three or more groups by the Kruskal-Wallis test with Dunn's post hoc test; P values are unadjusted for multiple comparisons. G) Three-gene risk score in the same cohort: patients with complete expression data for all three genes were ranked by ascending risk score and dichotomized at the cohort median of 0.0524 (upper); follow-up time and event status of each

902 patient, with events comprising refractory disease, relapse or histological transformation (middle); and
903 heatmap of z-scored SIRPG, FLT3LG and LAG3 expression across the same ranking (lower). H)
904 Kaplan-Meier analysis of event-free survival in the high- and low-risk groups defined in G; comparison
905 by log-rank test. I) Representative immunohistochemical staining of SIRPG, FLT3LG and LAG3 in
906 low-grade and high-grade FL; boxed areas in the left-hand images are shown at higher magnification
907 on the right. Staining was assessed descriptively and was not scored. Scale bars, 100 µm (left) and 50
908 µm (right). FL-IPI, Follicular Lymphoma International Prognostic Index.
909

910 **Table 1.** Summary of datasets used in this research.

Dataset	Platform	Sample size	Purpose	Reference
GSE182434 (Single Cell RNA Sequencing)	Illumina HiSeq 4000	6	Exploration	Steen CB et al. [41]
GSE66166 (bulk RNA Sequencing)	Illumina HumanHT-12 (GPL13938)	138	Construction	Pastore A et al. [14]
GSE119214 (bulk RNA Sequencing)	Illumina HumanHT-12 (GPL13938)	137	Validation	Silva A et al. [15]
GSE16131 (bulk RNA Sequencing)	Affymetrix Human Genome U133A/U133B Array (GPL96/GPL97)	180	Validation	Leich E et al. [57]

911

Fig. 1 [Download full resolution image]

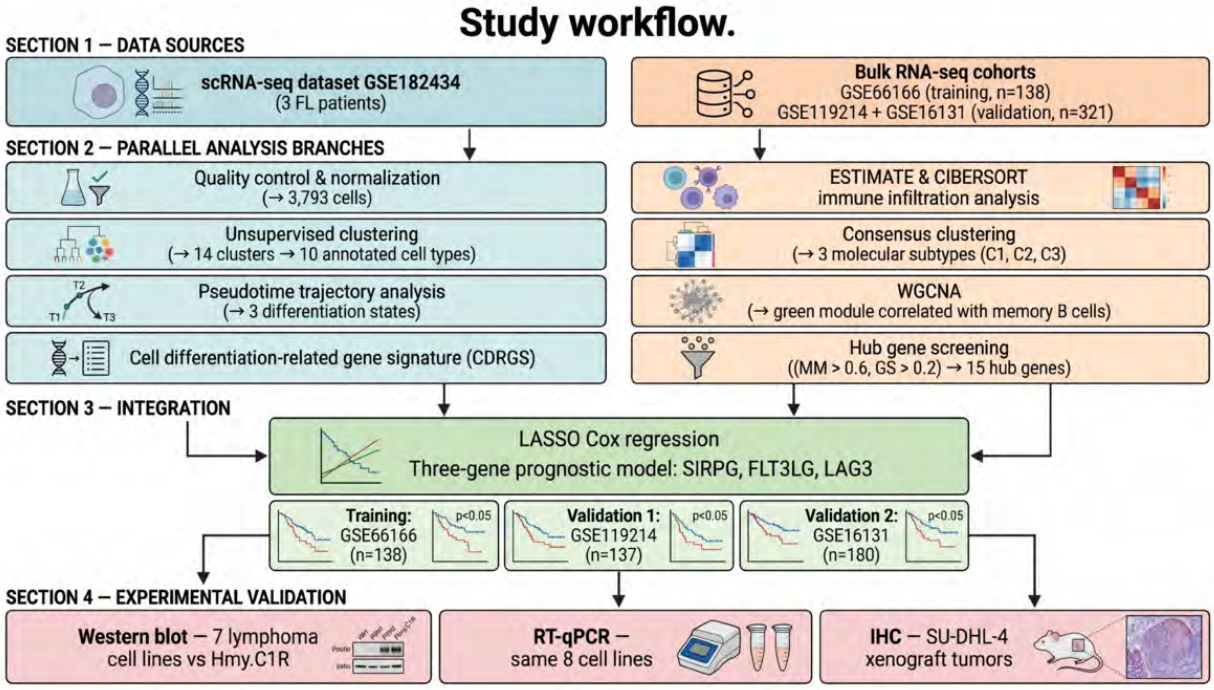

Fig. 2 [Download full resolution image]

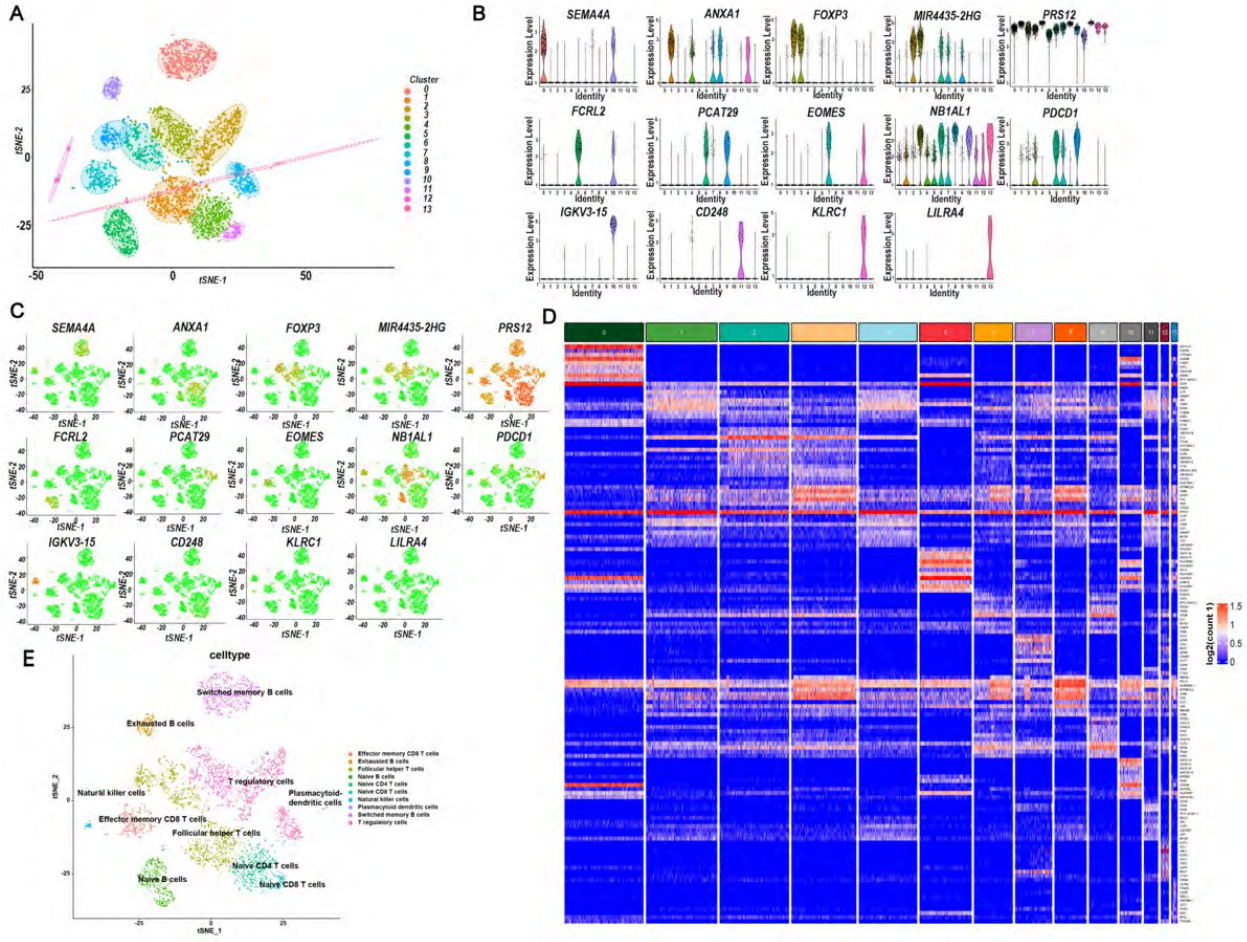

Fig. 3 Download full resolution image

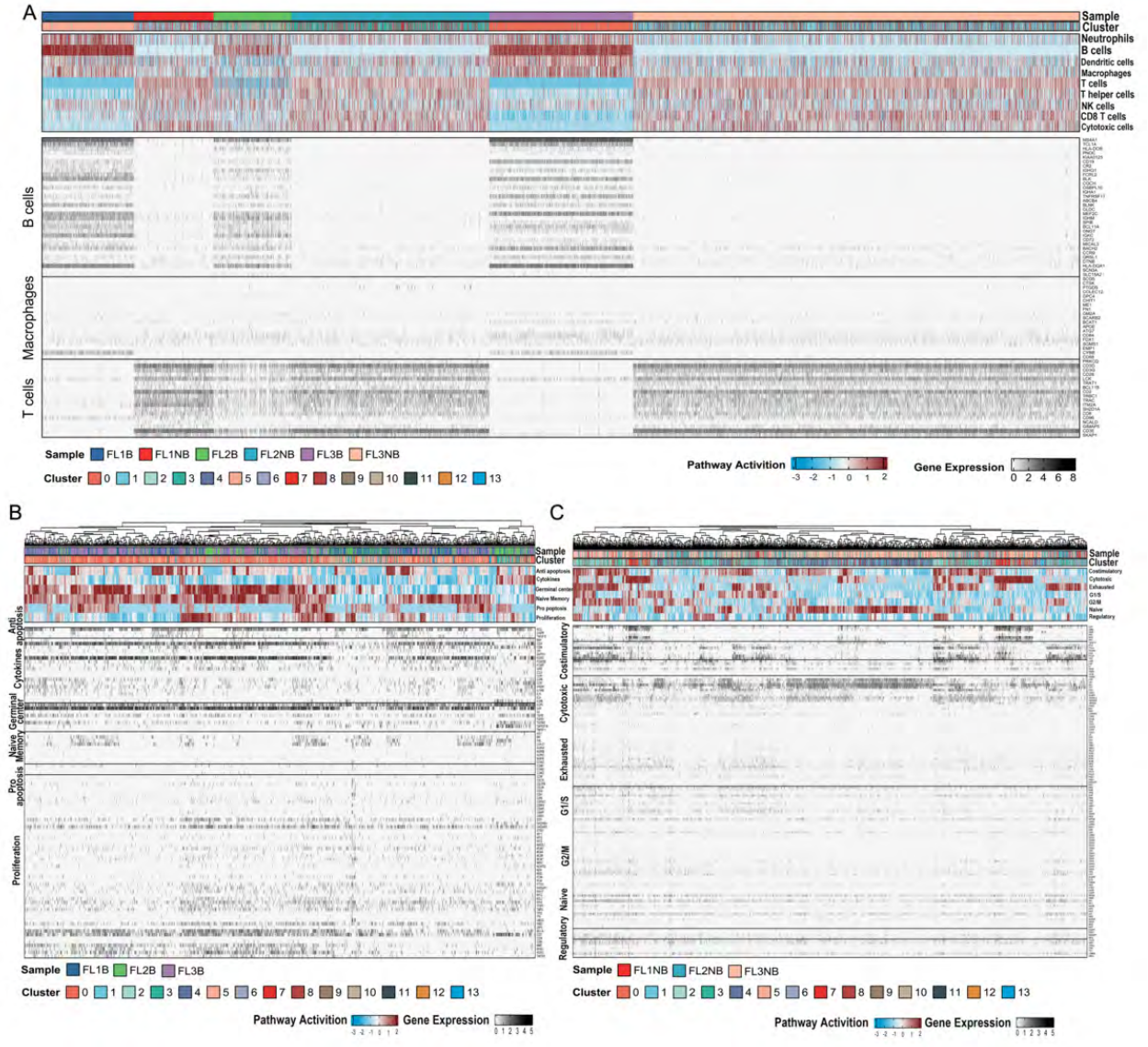

Fig. 4 [Download full resolution image]

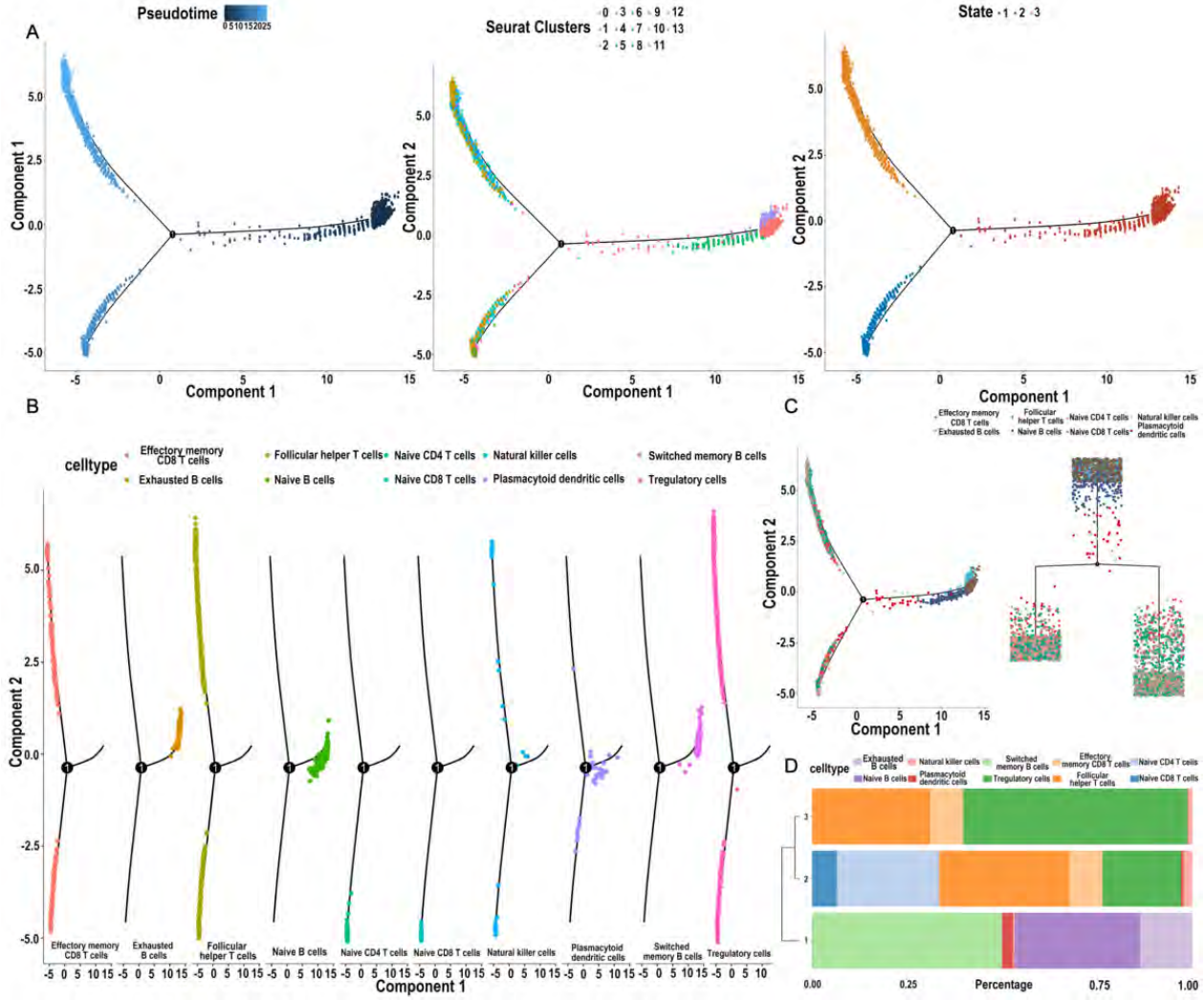

Fig. 5 Download full resolution image

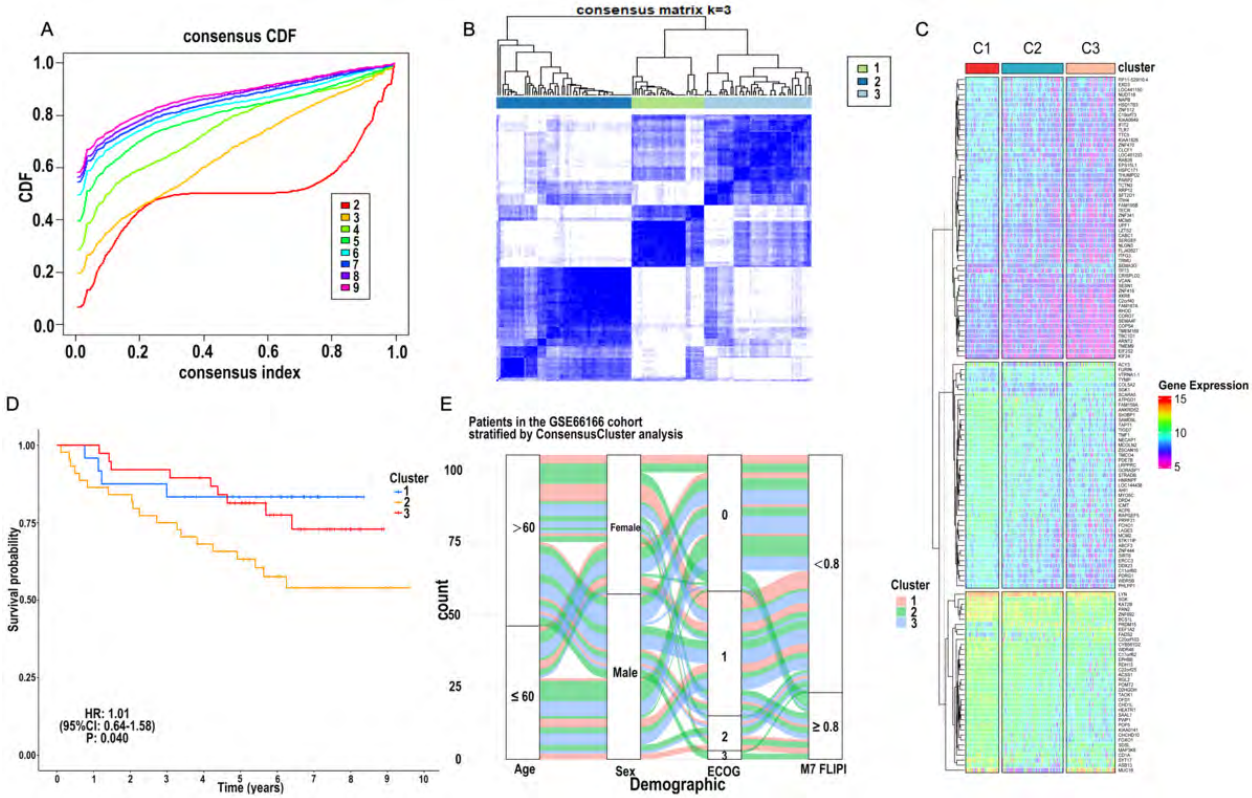

Fig. 6 [Download full resolution image]

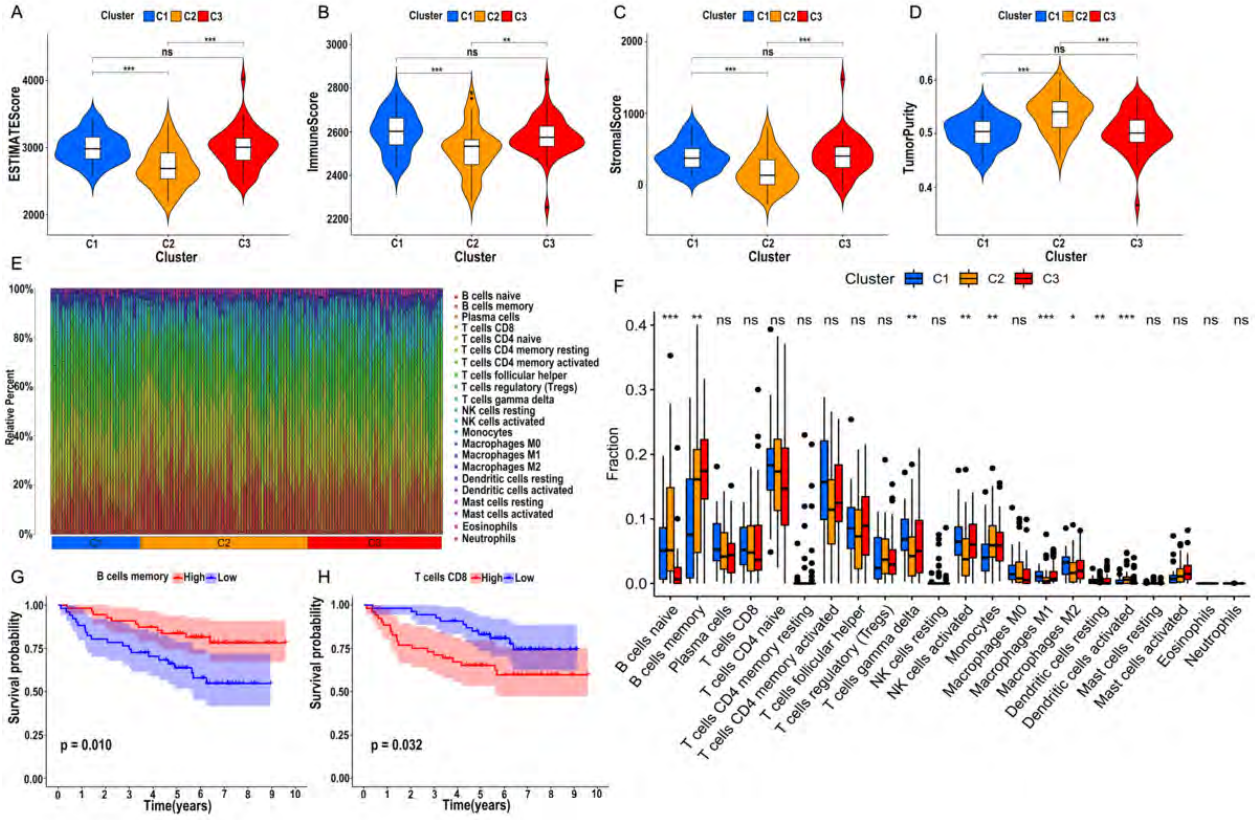

Fig. 7 Download full resolution image

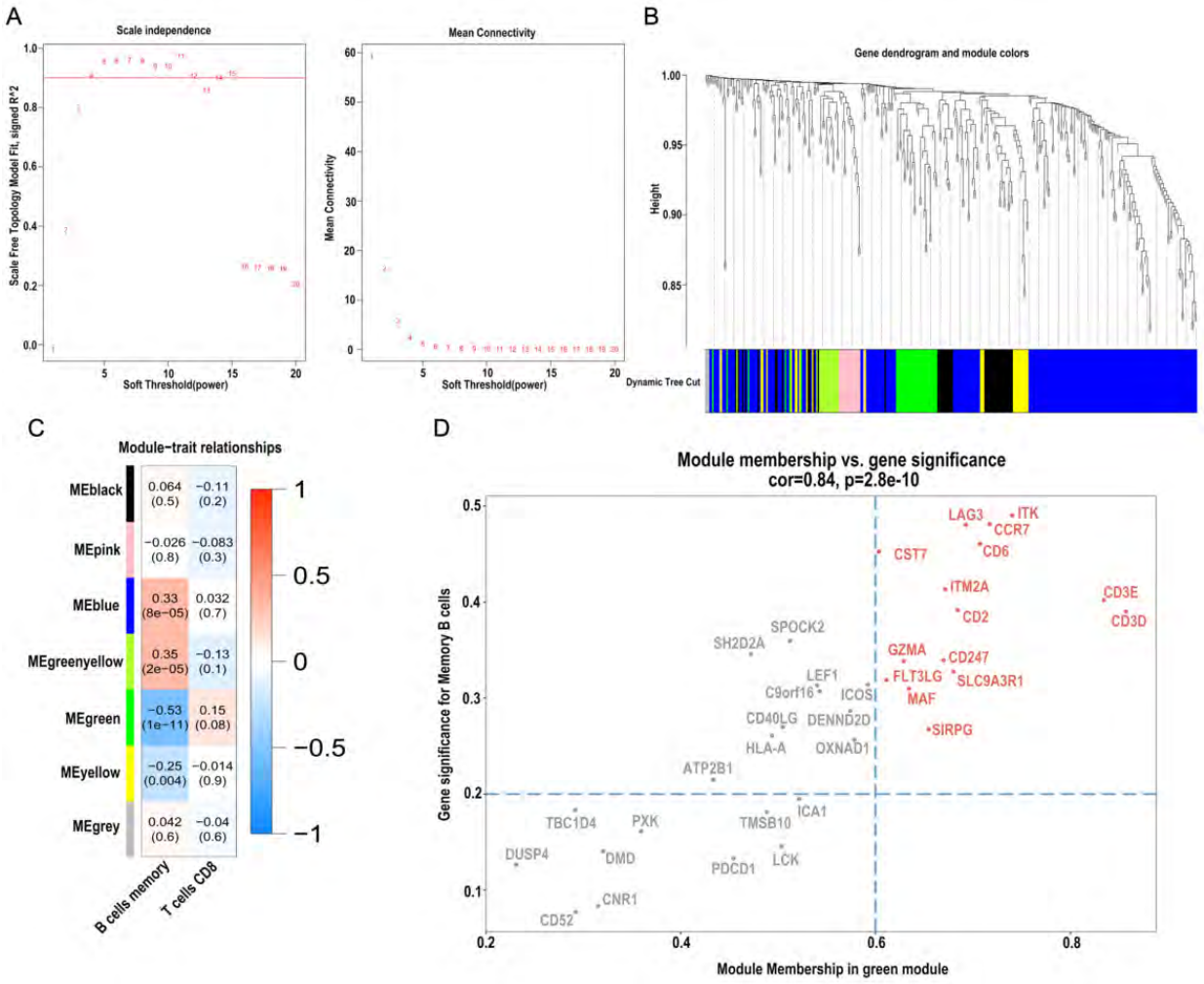

Fig. 8 [Download full resolution image]

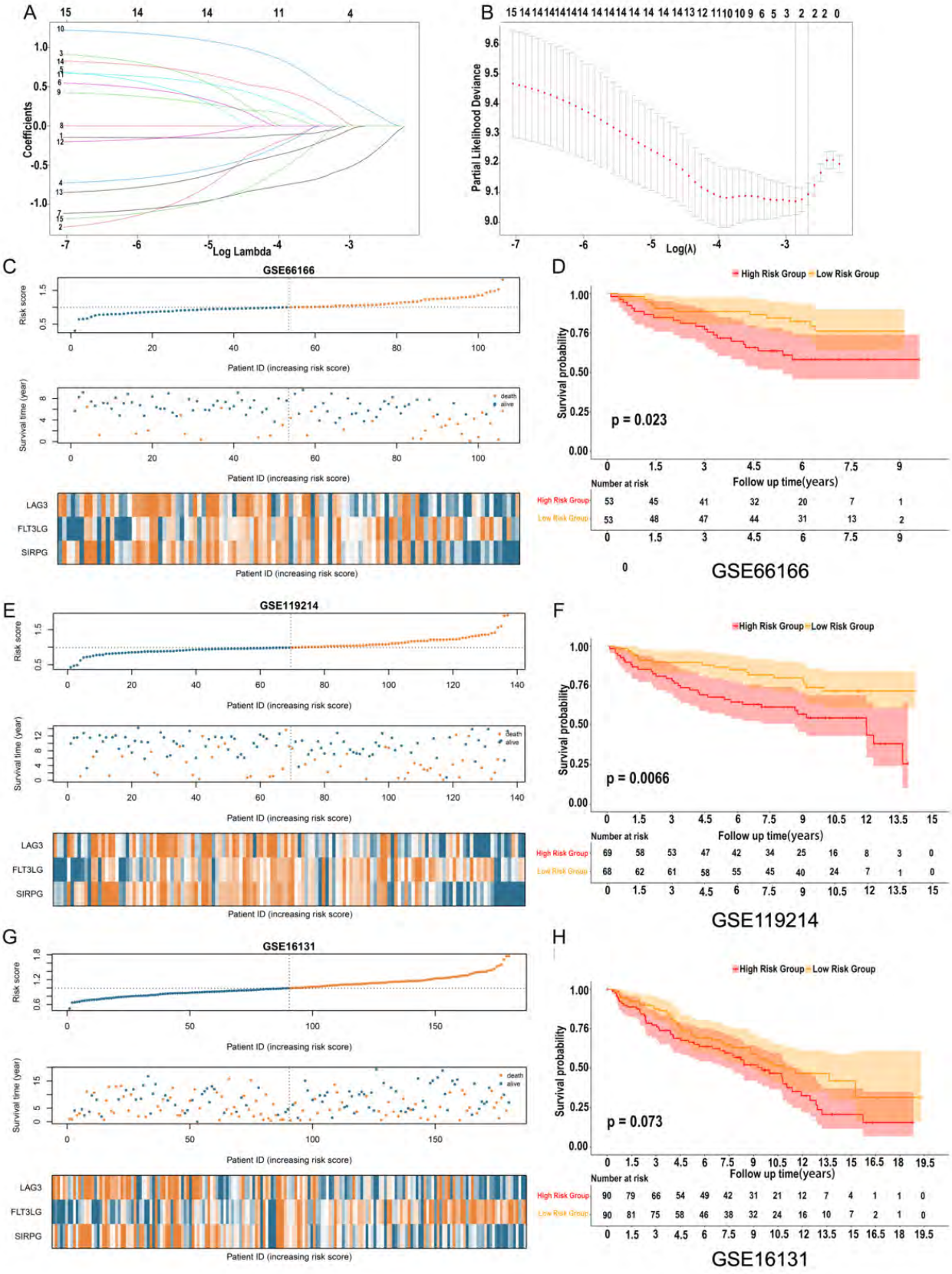

Fig. 9 Download full resolution image

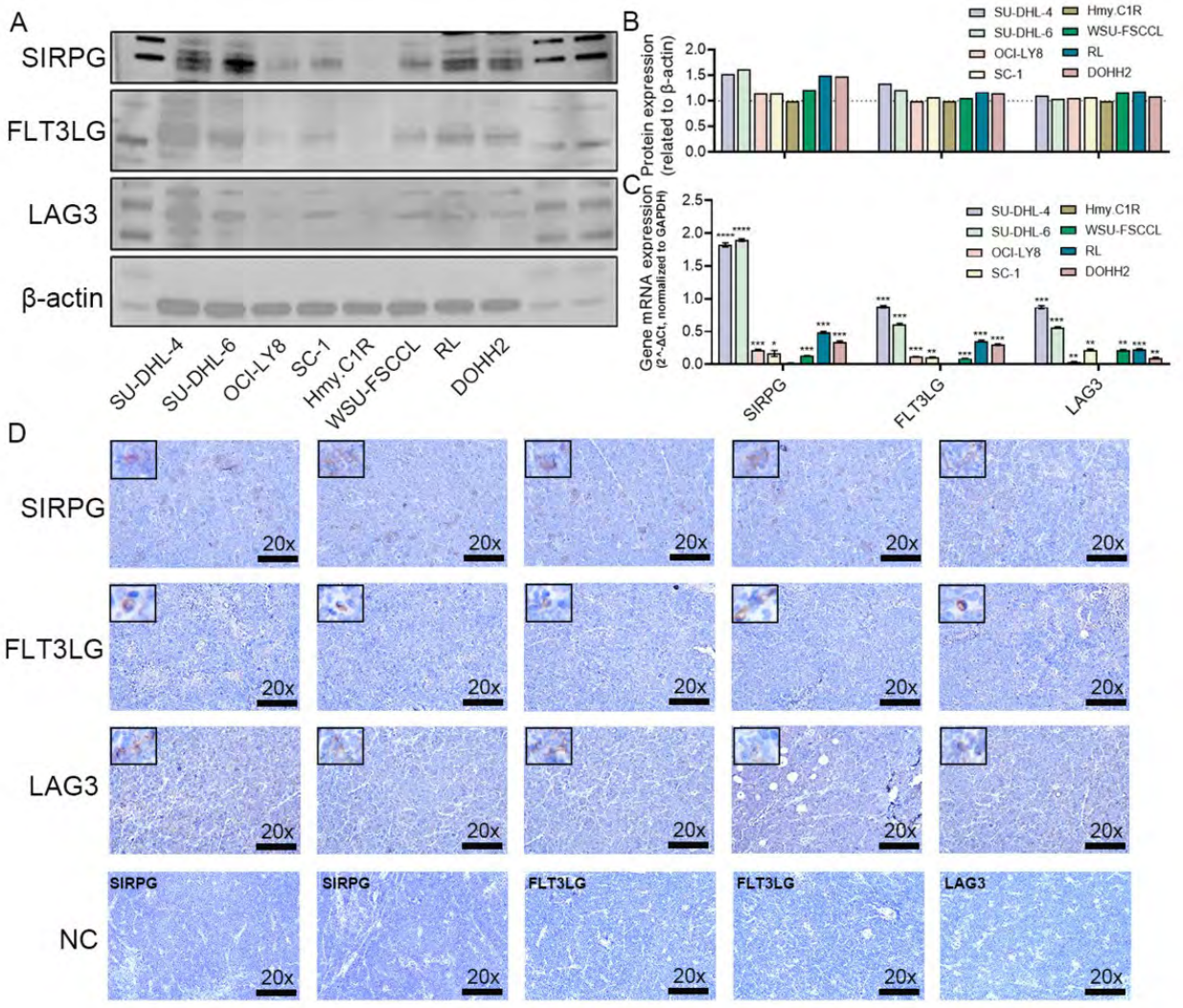

Fig. 10 [Download full resolution image]

